

PATTERNS OF TREE DEFOLIATION AND MORTALITY FROM INSECT
DAMAGE USING MULTI-SCALE REMOTE SENSING

By

LUKE WALTER SCHEFKE

A thesis submitted in partial fulfillment of
the requirements for the degree of

MASTER OF SCIENCE IN ENVIRONMENTAL SCIENCE

WASHINGTON STATE UNIVERSITY
School of the Environment

DECEMBER 2023

© Copyright by LUKE WALTER SCHEFKE, 2023
All Rights Reserved

To the Faculty of Washington State University:

The members of the Committee appointed to examine the thesis of LUKE WALTER SCHEFKE find it satisfactory and recommend that it be accepted.

Arjan Johan Herman Meddens, Ph.D., Chair

Henry David Adams, Ph.D.

Mark Ellyson Swanson, Ph.D.

ACKNOWLEDGMENT

I would like to thank my committee members Drs. Arjan Meddens, Henry Adams, and Mark Swanson for their consistent support throughout my time as a Master of Science student. I would also like to thank Dr. Amanda Stahl for her work, both as our drone pilot and for her dedication to processing the imagery afterwards. Immense gratitude to Benjamin Bright, Abhinav Shrestha, Dr. Jeffrey Hicke, and Dr. Andrew Hudak for their knowledge of forestry and assistance in collecting field measurements. Special thanks to those at the National Aeronautics and Space Administration (NASA) for providing funding for research involving small satellite technology (award number 80NSSC21K1155); this work utilized data made available through the NASA Commercial Smallsat Data Acquisition (CSDA) Program. To all the graduate students, faculty, and staff who I crossed paths with, your help both professionally and personally have proven invaluable.

PATTERNS OF TREE DEFOLIATION AND MORTALITY FROM INSECT
DAMAGE USING MULTI-SCALE REMOTE SENSING

Abstract

by Luke Walter Schefke, M.S.
Washington State University
December 2023

Chair: Arjan Johan Herman Meddens

With the climate rapidly changing, coniferous trees in North America face many threats, and both native and invasive insects are contributing to their decline and mortality. As insects, particularly bark beetles, successfully attack trees, the foliage of those trees undergoes a color shift from green to red to gray. Attacks from other insects, such as defoliators, can result in defoliation, crown thinning, and loss of needles. These changes may be detected by remote sensing instruments such as satellites and drones. Tree mortality may also come from multiple other variables, such as fire or drought, which then causes tree stress, making plants more susceptible to insect infestation.

I analyzed an area with tree disturbance and mortality from three distinct types of insects in Montana, United States to study the detection of forest disturbance by insect outbreaks. This study aims to examine the patterns displayed across a section of forest at different spatial resolutions and scales. Field studies consisted of measuring variables such as diameter, health, and needle color on both trees inside eight-meter fixed-radius plots as well as individual trees not within plots. I analyzed and classified imagery from various sensors, including data from an

unmanned aerial vehicle and multiple satellites. Pixels from these data sets are classified using two modeling techniques: maximum likelihood and random forest. This resulted in maps of different tree health classes and other land classes such as bare ground and herbaceous vegetation. I evaluated tree disturbance with classifications of finer spatial resolution pixels (subpixels), which were aggregated to the size of coarser spatial resolution pixels (superpixels) by calculating the percentage of unhealthy trees within, and then comparing them to the classification of the actual classified superpixels. By comparing classification results at different resolution levels, it is possible to extract what information was retained or lost at each step down in spatial resolution, and field measurements provided corroborating evidence of tree disturbance.

Random forest models outperformed maximum likelihood models based on accuracy of withheld evaluation points, with overall accuracies ranging from 81.5% to 94.5%. Corroboration of individual trees from the field data was only easily feasible with UAV data, plausible with WorldView-3 data, and not possible with any imagery of 10-m spatial resolution or coarser. Total percent area affected of unhealthy trees was not consistent across resolutions, although coarser imagery tended to underestimate mortality or damage for most intensities of finer imagery disturbance when grouped into distinct disturbance bins but predict more mortality or disturbance across an entire landscape. This study will assist forest managers and natural resource scientists in understanding detection of insect-affected forests, in particular when insect outbreaks are more diffuse and not severe across the entire landscape, giving managers guidelines for where to invest time and resources. This research will also allow for general trends for areas with insect-specific mortality, allowing for potential future comparisons with other causes of tree mortality.

TABLE OF CONTENTS

	Page
ACKNOWLEDGMENT.....	iii
ABSTRACT.....	iv
LIST OF TABLES	viii
LIST OF FIGURES	ix
INTRODUCTION	1
Global Forest Disturbance	1
Insect-Caused Disturbance.....	1
Spatial and Temporal Patterns of Disturbance.....	3
Tree Response to Disturbance Agents	3
Interaction Between Disturbance Agents.....	5
Available Data on Insect Outbreaks	6
Gaps in Research.....	9
Research Goals and Objectives.....	9
METHODS	16
Study Area	16
Field Measurements	19
UAV Data Collection.....	22
Satellite Data Collection	23
Remote Sensing Data Processing.....	27
Classification Models.....	29
Spatial Detection Analysis	32

RESULTS	35
Field Observations	35
Classification Models.....	39
Spatial Detection Analysis.....	45
DISCUSSION.....	51
Field Work	51
UAV Imagery.....	51
Satellite Imagery	52
Classification Accuracy and Importance	53
Patterns and Spatial Analysis.....	56
Caveats and Improvements	59
Management Implications.....	59
Comparisons and Future Research.....	60
CONCLUSION.....	62
Research Questions Revisited.....	62
Main Takeaways	64
REFERENCES	65
APPENDIX.....	77

LIST OF TABLES

	Page
Table 1: Selected insects and host of North America	12
Table 2: Field measurements and descriptions	22
Table 3: Summary of remote sensing data.....	29
Table 4: Field versus UAV tree health comparison.....	36
Table 5: Benefits, drawbacks, and management uses of sensors.....	56

LIST OF FIGURES

	Page
Figure 1: Examples of damage caused by insects.....	15
Figure 2: Study area within Lolo National Forest	18
Figure 3: Locations of plots and individual trees.....	21
Figure 4: General workflow summary for remote sensing processing	26
Figure 5: Percentage of green needles by tree species.....	37
Figure 6: Diameter at breast height by tree health status.....	37
Figure 7: Comparison between field measurements and remote sensing imagery	38
Figure 8: Sample of different sensors and classification models.....	41
Figure 9: Comparison of different sensors and classification models at fullest extent	42
Figure 10: Producer's accuracy by class and sensor and overall accuracy by sensor	43
Figure 11: Relative importance for band and index variables	44
Figure 12: Maps and histograms of MicaSense subpixels within different superpixels.....	47
Figure 13: Sentinel-2 classes compared to unhealthy tree WorldView-3 subpixel frequency	48
Figure 14: Landsat 9 classes compared to unhealthy tree WorldView-3 subpixel frequency	48
Figure 15: Sentinel-2 and Landsat 9 superpixel frequencies by WorldView-3 subpixel groups ..	49
Figure 16: Sentinel-2 and Landsat 9 unhealthy tree pixels moving window analysis.....	49
Figure 17: Percentage unhealthy trees out of total and out of classified forest pixels.....	50
Figure 18: Producer's and user's accuracy compared to spatial resolution of sensor	56

Dedication

To my family, both of origin and of choice

INTRODUCTION

Global Forest Disturbance

Disturbance events across forest ecosystems are global phenomena. These disturbances are caused by (1) direct anthropogenic factors, such as deforestation and conversion to agricultural or residential land use that can eliminate forests entirely (Curtis et al., 2018), (2) indirect anthropogenic factors, namely climate change from the anthropogenic release of carbon dioxide through the burning of fossil fuels, increasing the global temperature and changing regional weather patterns (Hammond et al., 2022), (3) abiotic factors, such as fire and floods that may simply return forests to early seral states (Swanson et al., 2014), and (4) biotic factors, such as insects, fungi, and diseases that may not cause forest-wide mortality and mainly advance ecosystem succession (MacLean, 2016). These disturbances are important to observe and quantify, as they impact biogeochemical cycles (Cigan et al., 2015) as well as the ecosystem services that forests provide (Andregg et al., 2016).

Insect-Caused Disturbance

One specific biotic cause of disturbance, examined here in detail, is that of tree-damaging insect species, which vary by region and ecosystem. These insects can be split into three main groups (or guilds): bark beetles, defoliators, and sap suckers (Figure 1; Table 1). The first category of insects, bark beetles, includes species such as mountain pine beetle (*Dendroctonus ponderosae*), western pine beetle (*Dendroctonus brevicomis*), Douglas-fir beetle (*Dendroctonus pseudotsugae*) and spruce beetle (*Dendroctonus rufipennis*) (Hadney & Veblen, 1992). Bark beetles attack the woody organs of the tree in an attempt to overwhelm tree defenses. Beetles burrow to feed on the plant tissues underneath the bark in boles or branches. There they then

breed and provide nutrition to their larvae using primarily the phloem and cambium layers (Furniss & Carolyn, 1977). Damage from beetle attacks results in a stress response by the tree (see below) and often, but not always, leads to mortality of a tree once an infestation has begun. The number of beetles that attack and how quickly they attack depends on species behavior, as most beetles release pheromones that function as chemical signals to either attract or repel other beetles to host trees (Windmuller-Campione et al., 2021).

Defoliators, such as the Douglas-fir tussock moth (*Orgyia pseudotsugata*) and western spruce budworm (*Choristoneura freemani*), consume or strip needles from trees. For western spruce budworm, this involves their larvae feeding on new needle growth (Senf et al., 2015), leading to crown thinning or patchiness. An individual tree may experience several cycles of defoliator attacks during its lifetime, as trees are generally not killed during defoliator outbreaks and then regrow their needles after insect population collapse (Senf et al., 2017). If defoliation events are severe for several consecutive years, carbon reserves might become depleted, leading to eventual tree mortality (Alfaro et al., 1986).

The last category of these threats is that of sap-sucking insects, such as the balsam woolly adelgid (*Adelges piceae*). These insects are microscopic (Campbell et al., 2023), substantially smaller compared to the species previously mentioned. They are known for their tomentose protective structures produced as they mature as well as very sporadic patterns of tree injury or mortality (Campbell et al., 2023). All three categories have different primary and secondary hosts (the former are trees that are mainly affected by the insect, the latter are trees that may be impacted but less commonly), yet all of these insect disturbance categories are present in the western United States over the past twenty years.

Spatial and Temporal Patterns of Disturbance

In North America, various tree species across the western United States have experienced significant levels of decline over the past few decades (Edburg et al., 2012). This includes extensive lodgepole pine (*Pinus contorta*) mortality in the Rocky Mountains and evergreen forest mortality extending into British Columbia, Canada (Meddens et al., 2012; Mikkelsen et al., 2013). Bark beetles are responsible for the majority of this decline; when conditions are favorable (e.g., drought, stand structure, previous insect presence), some of these populations can move from an endemic to an epidemic population level and affect large areas of coniferous forests (Meddens et al., 2012). During the 20th century, western white pine forests decreased in both area and connectivity across northwestern Montana, partially from mountain pine beetle attack (Hessburg et al., 2000). In the United States, both mountain pine beetle and western spruce budworm (i.e., both a bark beetle and a defoliator) have seen a resurgence in their populations since at least the year 2000, with an outbreak for the latter in western US states as of a decade ago (Hicke et al., 2012). In British Columbia, western spruce budworm has an approximately 28-year reoccurrence cycle (MacLean, 2016). Between 1975 and 2000, spruce budworm in Canada alone was responsible for at least 400 million acres of moderate to severe defoliation (MacLean, 2016). In all, the United States and Canada, particularly their western-most contiguous regions, have experienced areas of extensive forest ecosystem change as a result of high-level insect disturbance.

Tree Response to Disturbance Agents

Trees produce visual indications of defense, damage, and eventual mortality caused by insects. Trees can attempt to repel insect attacks by producing chemicals known as secondary

metabolites (Huang et al., 2020), as well as produce pitch tubes in an attempt to force out insects, that both serve as evidence of attack (Cigan et al., 2015). Tree mortality occurs when the xylem and phloem network is sufficiently cut off around the entire circumference of the tree, girdling the tree and preventing sufficient water and nutrient flow (Andregg et al., 2015). After a successful infestation, conifer trees affected by tree-killing bark beetles generally undergo a spectral change, with needles transitioning from healthy and green (called green attack when insects are present) to red in color approximately one to four years after attack (Mikkelsen et al., 2013), when the tree is said to be in the red attack stage. After four years, trees appear gray as the red needles fall off the trees and fine twigs and branches become visible, commonly referred to as gray attack (Meddens et al., 2011; Hicke et al., 2012). For defoliators, their damage also results in visible changes to tree color; however, this spectral change can be short-lived (Rhodes et al., 2022) and variable (Senf et al., 2015), as trees, if not killed, can recover, and they can regrow any damaged or lost needles within five years.

Forests as a whole are affected as well, with beetle attacks in lodgepole pine inducing a decrease in transpiration beginning at the green attack stage followed by increases in soil moisture during the red attack stage (Edburg et al., 2012). Dramatic increases in evaporation occur at the gray stage, then evaporation decreases to below baseline rates during regrowth. Insect outbreaks affect forest functioning, including, but not limited to, carbon cycling (Kurz et al., 2008), timber production (MacLean, 2016), water resources (Adams et al., 2012), and cultural or aesthetic integrity (Breshears et al., 2011). These insects can also impact forest growth and functioning, as tree mortality can lead to a decrease in gross primary productivity, an increase in surface water runoff and subsequent streamflow, and an increase in respiration caused by leaf decomposition (Anderegg et al., 2016).

Interaction Between Disturbance Agents

There is a complex interplay between insect-related mortality and other mortality factors (Allen et al., 2010), as stress from one disturbance agent can cause a tree to be more susceptible to another problem that, on its own, may not lead to mortality. For example, drought stress can lead to a tree mortality event through either direct water loss in the xylem tissue, limits induced on a tree's capability to defend against disease or pests, or the drought-associated increased temperatures leading to more overall disease and pests (Parker et al., 2006; Huang et al., 2020). Insect attacks, whether from defoliators or bark beetles, often co-occur with extremes in climate (Hessburg et al., 2000). Beetle attacks also change the way in which other species in the forest interact with trees that have served as insect hosts, as fungi species can capitalize on the damaged trees and galleries, distinct hollow tubes inside a tree used for movement and reproduction, left by the beetles (Windmuller-Campione et al., 2021). The inverse relationship may also affect forests, as trees damaged by fungi (causing white rot or brown rot) can then become more susceptible to subsequent beetle infestation (Parker et al., 2006). Changing climate patterns impact trees through moisture and temperature fluctuations, as mentioned earlier, but also by the changing disturbance regimes of insects and diseases (Allen et al., 2010). Across the western United States, a combination of previous human-driven fire management techniques as well as an increase in average temperatures are expected to result in an increase in burned area per year, as well as an expanded fire season (Dello, 2017). In the 20th century, fire management often involved complete suppression of wildland fires, resulting in higher carbon storage within forest ecosystems (Tilman et al., 2000). When fires then do occur, this available carbon can then increase the intensity and severity of the subsequent fires (Baker, 1994). However, the

relationship between insect outbreaks and wildfire risk does not always follow a clear pattern, as while insect-related mortality increases the abundance of forest floor fuels over time, the risk of crown fires increases during the red attack stage but then is reduced during and after gray attack (Hicke et al., 2012).

Available Data on Insect Outbreaks

An important resource for monitoring bark beetle or defoliator outbreaks, and tree mortality more broadly, are insect and disease detection surveys (IDS) from the US Department of Agriculture's United States Forest Service (USFS), which conduct annual visual assessments of forest health (<https://www.fs.usda.gov/foresthealth/applied-sciences/mapping-reporting/detection-surveys.shtml>). The IDS data is available for most forested areas, separated out into different regions across the United States. IDS data is collected on an annual basis by trained observers in fixed-wing aircraft that observe targeted areas and manually mark regions of tree defoliation or mortality. For a given flight, a surveyor in an aircraft digitally marks areas of visible forest damage, with multiple variables recorded such as percent of trees affected, host tree species, and likely mortality agent. While flying aircrafts to survey areas may be helpful in some situations, it is also expensive, prone to human error, and can be interrupted by other events, such as in 2020 with the impacts of the COVID-19 pandemic.

Another source of information, remote sensing via digital sensors, has been used to monitor ecosystem health for over half a century (Wang et al., 2010), and consists of a wide range of imaging capabilities. Available satellite data ranges in spatial resolution from coarser-scale MODIS (240-m to 1000-m spatial resolution) to moderate-resolution Sentinel and Landsat (10-m to 60-m spatial resolution), to commercial, fine spatial resolution satellites (1-m to 5-m

spatial resolution) (Rhodes et al., 2022). More recent developments have led to unmanned aerial vehicles (UAVs) flying with sensors of very fine resolutions (less than 1-m spatial resolution) (Bergmüller & Vanderwel, 2022).

Remote sensing instruments usually record data in a series of bands, representing different ranges of the electromagnetic spectrum. These bands represent the wavelengths or energy levels that sensors on the satellite are able to detect and record and can be useful for monitoring forest health (Immitzer et al., 2012). The number of bands a sensor is able to record is referred to as its spectral resolution. Different devices record in different ranges, often covering a span from visible light to near-infrared or shortwave infrared. For each band, the instrument collects data in discrete segments called pixels. These are usually square in shape and contain the average band values within the area of the pixel. The length of one side of a pixel is used to describe the spatial resolution of a remote sensing technique. However, remote sensing almost always comes with tradeoffs, such as higher resolution imagery that can capture more detail (e.g., effects on individual trees) having a lower revisit frequency (Durgen et al., 2020). Remote sensing projects often must contend with balancing spatial resolution, spectral resolution, temporal resolution (i.e., time between scans) and overall resource cost.

The previously mentioned spectral shift of trees (green to red to gray), due to needles changing color and then being lost from the tree entirely, can be detected using remote sensing imagery. Moderate resolution imagery has previously been used to detect forest disturbance from insects. Wulder et al. (2006) used Landsat 7 data to estimate the likelihood of an area experiencing mountain pine beetle attacks. They examined the use of an enhanced wetness difference index (EWDI) as well as other predictors related to topographic features to generate a probability of red trees being present and related to beetle damage. Other studies have also used

moderate-resolution Landsat data, using a series of images across a set amount of time (Meigs et al., 2011) or comparing a single image to multitemporal data (Meddens et al., 2013). Defoliator detection has also been attempted using Landsat data, although not as successfully as beetle surveys, since, as previously stated, areas with defoliators tend to undergo less intense spectral changes (Senf et al., 2015).

Satellites with higher resolutions, in the 1-m to 5-m range, have been used to map the distribution of certain habitats and geographic features (Belgiu & Drăguț, 2016). QuickBird, with a multispectral spatial resolution of approximately 2.4 m, has been used to evaluate the change in forest health over time due to beetle attack, specifically looking at the red and green reflectance values (Wulder et al., 2008). Calculated spectral values were also compared with field measurements, shown to have a relatively high accuracy in matching data points. Even higher resolution techniques, such as those mounted to aircraft, have been used in studies attempting to examine specific changes in tree crown features (Coops et al., 2003) or general vegetation mapping (Wulder et al., 2006).

UAVs, with even higher resolution than any available satellite, have previously been used to monitor the health of agricultural lands (Turner et al., 2011) and to organize information on the human-built environment (Zhou et al., 2018), but this mapping can also be extended to mapping forest ecosystems. UAVs have been used to incorporate multivariate modeling with and without spectral indices. However, both types of models resulted in significant overestimation of tree mortality when used in forests known to be affected by mountain pine beetle in western Canada (Bergmüller & Vanderwel, 2022). Overall, remote sensing and subsequent modeling have already proven to be a useful tool in forest health analysis with wide range of uses, from plant stress to biomass surveys to general classification (Wang et al., 2010). Detecting visual

cues from insect-caused tree disturbance is an important aspect of the evolving world of remote sensing.

Gaps in Research

Using satellite technology has the potential to improve forest disturbance detection, but more investigation is needed into what traits and patterns remain at different scales. Many studies on forest effects resulting from beetle outbreaks have already been conducted, but the impacts of defoliators are not as well documented, with only a few studies being conducted on coniferous defoliators in western North America (Senf et al., 2017). Additionally, it is important to assess what patterns are retained and what is lost when moving from finer to coarser spatial resolution imagery. Previous studies have focused on a single type of imagery (Coops et al., 2003; Wulder et al., 2006; Wulder et al., 2008), but analysis of each separate image is important for validating potential uses and improvements to research protocols. Insect-affected individual trees are well captured in high-resolution (< 3-m) data (Meddens et al., 2011), however it is not clear at which level or spatial arrangement moderate resolution data can detect this disturbance and what might lead to under or overestimation of the affected areas. This leads to a need to quantify what tree disturbance moderate-resolution data might omit or overestimate. Fully understanding detection capabilities of data of different spatial resolutions will prove even more valuable as species shift and adapt to a changing climate, which can result in changes in severity or frequency of other stressors such as wildfires, droughts, and floods.

Research Goals and Objectives

This multifaceted problem of declining tree health makes it difficult for natural resource scientists and land managers to determine the best course of action (e.g., the selection of the most appropriate sensor or available data to analyze and plan management actions) when forest disturbance is occurring. The future of forest management depends on assessing these risk factors across space and time to determine the state of ecosystems. Natural resource managers and other scientists need accurate surveys to make informed decisions, and can utilize data from mapping, aerial assessment, and other remote sensing techniques. For this study, I examined one of the main causes of forest health issues and dieback in North America: attacks and infestations of trees by insects. This research attempts to understand the utility and accuracy of remote sensing data to detect the health of individual trees and tree stands in areas known to be affected by insects. Here, I seek to study the benefits and shortcomings of different spatial resolutions, specifically with regards to insect damage detection. I specifically examined the Intermountain West region of North America with a case study near Missoula, Montana, USA.

The overall objective of this thesis is to compare and assess insect damage detection in an area located near outbreaks of the three major groups of insects listed above. My subobjectives are to (1) determine composition and disturbance patterns of the forest inside the study area, (2) classify and evaluate UAV images using on-screen class member selection and field observations, (3) classify satellite images using an on-screen class member selection, using higher resolutions to help classify lower resolutions if necessary, and (4) compare and contrast accuracy and disease detection patterns across the scales, models, and spatial or spectral resolutions assessed. In order to accomplish and draw inferences from these subobjectives, I proposed the following research questions: (1) What species and size of tree are most affected in the study area, and how well does field data match with UAV data? (2) Is a parametric or non-



parametric model better at classifying remotely sensed forest health? (3) How does spatial resolution affect classification model accuracy? (4) What spectral bands or indices are most important in classification? (5) Are coarser resolution satellites overestimating or underestimating disturbance, and if so, at what thresholds? (6) Are landscape metrics consistent across spatial resolutions and scales? (7) What are the benefits and drawbacks of different sensors, based on the answers to the previously described research questions? For these research questions, I hypothesized that (1a) subalpine fir and lodgepole pine will be most affected based insects present in the study area, (1b) the largest trees will be most affected or already dead, due to previous disturbance, as insects may have a preference for larger trees, and (1c) field data of unhealthy trees will correspond to tree health determination from on-screen UAV data.




Additionally, I predicted that (2) a non-parametric model will be better at classifying forest health, (3) finer spatial resolutions will result in higher classification accuracy, and (4) the normalized difference vegetation index (NDVI), as well as red and near-infrared (NIR) bands individually, will be most important across resolutions. Finally, I propose that (5) a plot of superpixel bins of subpixel unhealthy tree frequency versus frequency of superpixel unhealthy tree classification will follow a sigmoid distribution, with low values of subpixel disturbance matching low frequency of unhealthy tree-classified superpixels and an inflection point at approximately 50% unhealthy tree superpixels (i.e., underestimation to overestimation), and (6) total percent unhealthy trees and percent unhealthy trees out of all pixels classified as forest will be consistent across resolutions.



My research involves a hierarchical classification approach, from field data to UAV data, to high-resolution satellite data, to moderate-resolution satellite data. Field data is used to obtain a general overview of the state of the forest in question, and then can be compared to UAV data

to compare how well a UAV could replace or supplement field surveys. UAV data is then nested within and compared to satellite data, and all this imagery is compared across their different spatial and spectral resolutions, in order to see what spatial patterns are present, what variables are important, and how sensors compare.

Table 1. Selected insects of interest of western North America, sorted into three guilds, along with notable primary and secondary hosts (latter being trees that may be attacked but are less likely to experience infestation), if applicable. Information on hosts from Forest Insect & Disease Leaflets (<https://www.fs.usda.gov/foresthealth/publications/fidls/index.shtml>) produced by the US Forest Service. All photos, except for western spruce budworm and balsam woolly adelgid, are from the Bugwood Image Database System; individual credit given.

Insect Guild	Photo Reference	Insect Species	Primary Host(s)	Secondary Host(s)
Bark Beetles	 <p data-bbox="461 1203 893 1276">William M. Ciesla, Forest Health Management International</p>	Douglas-fir beetle	Douglas-fir	-
	 <p data-bbox="461 1728 893 1801">Whitney Cranshaw, Colorado State University</p>	Mountain pine beetle	Lodgepole, ponderosa, western white, limber, and whitebark pine	All other pines within range

	 <p>Erich G. Vallery, USDA Forest Service</p>	Western pine beetle	Ponderosa and Coulter pine	-
Bark Beetles	 <p>Edward H. Holsten, USDA Forest Service</p>	Spruce beetle	All spruce within range (including white and Engelmann spruce)	-
Defoliators	 <p>William M. Ciesla, Forest Health Management International</p>	Douglas-fir tussock moth	Douglas-fir, true firs (including grand fir)	Colorado blue and Engelmann spruce

<p>Defoliators</p>	 <p>David G. Fellin and Jerald E. Dewey, USDA Forest Service</p>	<p>Western spruce budworm</p>	<p>Douglas-fir; grand and subalpine fir, Engelmann spruce</p>	<p>Mountain and western hemlock; lodgepole, ponderosa, and whitebark pine</p>
<p>Sap-Sucking Insects</p>	 <p>R.G. Mitchell, USDA Forest Service</p>	<p>Balsam woolly adelgid</p>	<p>True firs (including subalpine, Pacific silver, and grand fir)</p>	<p>-</p>

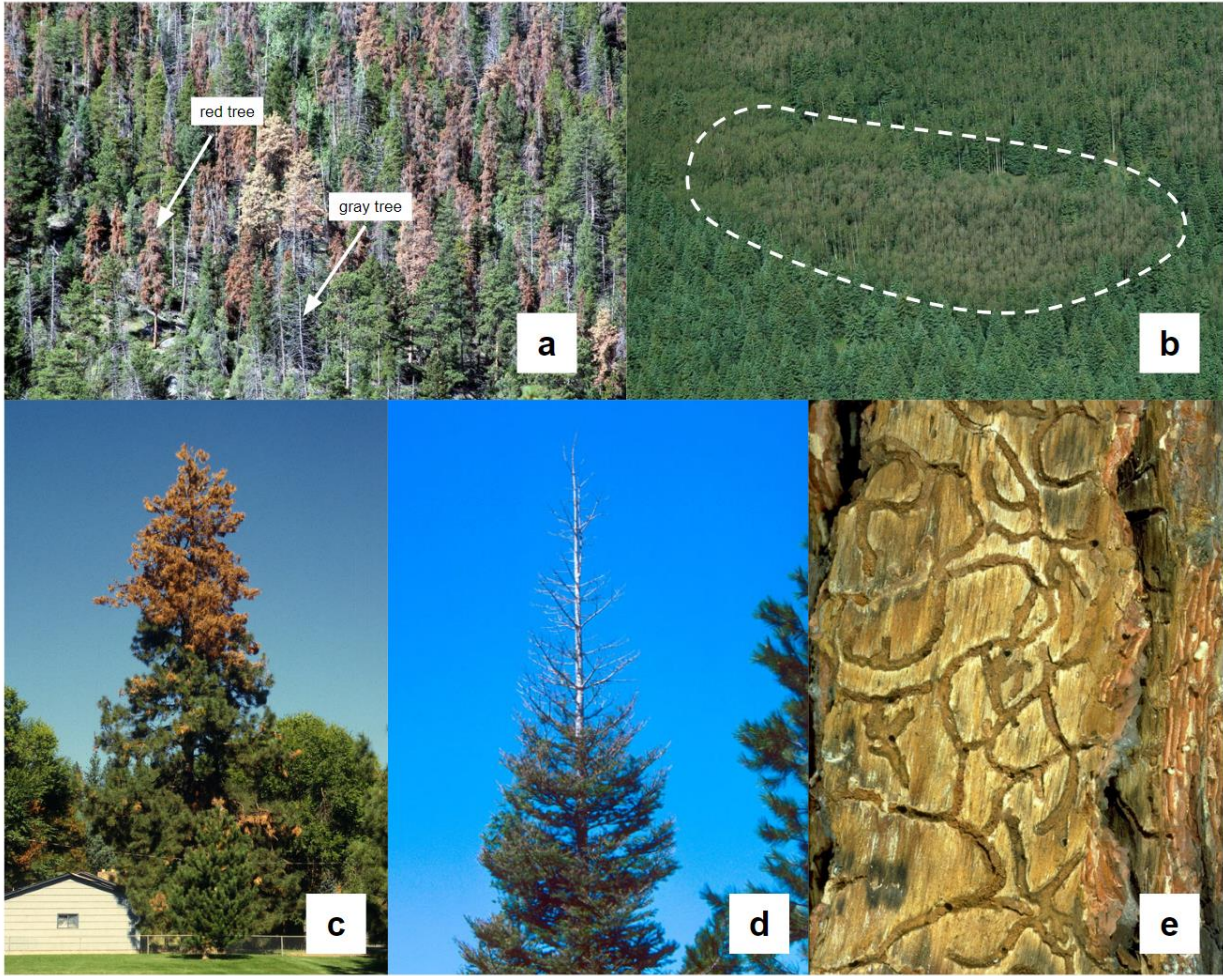


Figure 1. Examples of damage caused by insects (species not specified). All images from the Bugwood Image Database System. Shown here are (a) fully red and gray trees (Whitney Crenshaw, Colorado State University), (b) a large patch of defoliated trees (William M. Ciesla, Forest Health Management International), (c) a tree partially affected with red needles (USDA Forest Service, Coeur d’Alene Field Office), (d) complete topkill (Dave Powell, USDA Forest Service), and (e) beetle galleries underneath bark (Ladd Livingston, Idaho Department of Lands).

METHODS

Study Area

The study area was located in the Lolo National Forest, in the region around Sheep Mountain, northeast of Missoula, Montana, USA (Figure 2). This is an area with moderately to highly mountainous terrain, with silty or sandy loam (Linder et al., 1994) as well as gravelly loam (Lewis et al., 2017) soils. East Twin and West Twin creeks run through the northeast quadrant and southern half of the study area, respectively. This region contains intact, dry to moderately moist mixed-conifer forest (Pederson et al., 2010; Lewis et al., 2017), with precipitation averaging approximately 123 cm per year and a mean annual temperature of 4.1°C (30-year normal, Oregon State University PRISM). These forests also support key North American fauna, such as brown bears and gray wolves, however climate change has already increased stress on these ecosystems, with an increase of days above 32.2°C (Pederson et al., 2010).

To select the location of the study area, I used recent IDS polygons (USFS Mapping & Reporting, Region 1, from 2018 to 2022) that contained information on tree mortality and disturbance from insects. I considered insect disturbance type (from defoliators, bark beetles, and/or sap-sucking insects), severity, timing, and location from the IDS data, as well as field accessibility for ground observations and UAV data acquisition. The final selected area was easily accessible, and the region within and around the study area showed relatively recent (from 2018 or later) and widespread damage according to IDS data (Appendix Figure 1, referred to as Figure A.1) from defoliators, specifically western spruce budworm (*Choristoneura freemani*), and sap-sucking insects, namely balsam woolly adelgid (*Adelges piceae*). In addition, the study

region was affected by mountain pine beetles (*Dendroctonus ponderosae*) in 2011, and trees that were affected or killed by this outbreak are likely still-standing snags (gray-attack stage).

Data from field measurements and an unmanned aerial vehicle (UAV) were collected at this location, and imagery from three different satellites was available or requested for this area. The UAV data covers a small portion of the study area in two swaths of coverage, while the satellites provide mostly to entirely complete coverage (Figure 2). Evergreen coniferous tree species present in the study area were lodgepole pine (scientific name *Pinus contorta*, abbreviated as PICO), subalpine fir (*Abies lasiocarpa*, ABLA), Engelmann spruce (*Picea engelmannii*, PIEN), Douglas-fir (*Pseudotsuga menziesii*, PSME), and ponderosa pine (*Pinus ponderosa*, PIPO). Western larch (*Larix occidentalis*, LAOC), a deciduous evergreen, was also observed.

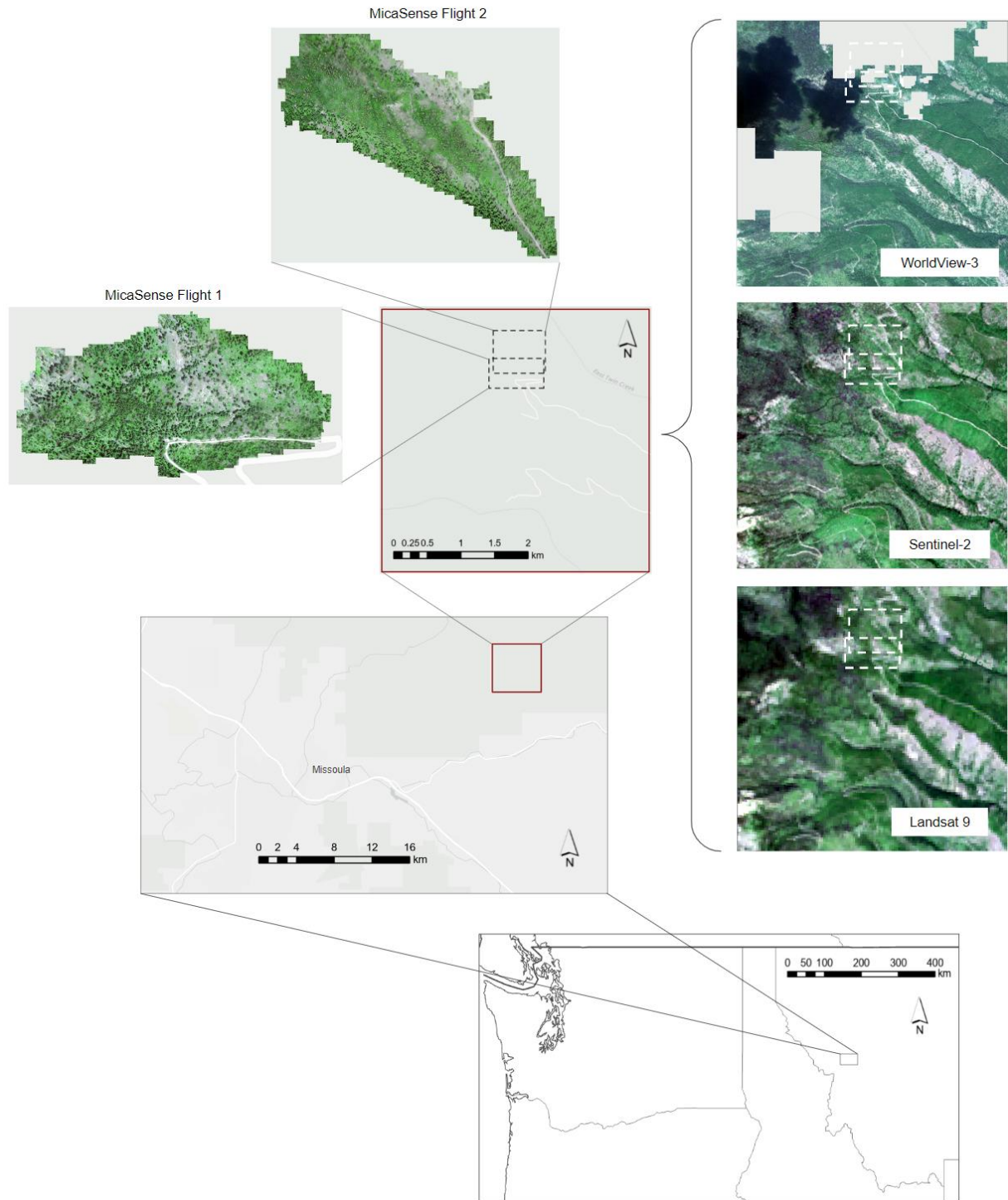


Figure 2. Study area within Lolo National Forest, examined due to high mortality and a large data set. Detailed location and cropping extent of the following imagery used are shown here: MicaSense Flights 1 and 2 (~ 0.1 m spatial resolution) after masking distortions, WorldView-3 (2 m; ©2022, Maxar, USG Plus) after masking clouds, Sentinel-2 (10 m), and Landsat 9 (30 m).

Field Measurements

From June 28 to June 30, 2022, I supervised a field crew and recorded trees in the field in two separate ways (Figure 3).

(1) We collected data across 18 semi-randomly placed eight-meter fixed-radius plots, each with an area of 200 m² (stand-level analysis). We examined health statuses of all mature trees (diameter at breast height ≥ 10 cm) within each plot ($n = 276$ trees). Trees within the plot were numbered (Table A.1) and their characteristics were recorded (Table 2). Before visiting the field site, a large number of potential plots were randomly placed on previously obtained, public satellite imagery, then these plots were sub-selected for crew visits while ensuring a diverse range of conditions (damage intensity, forest density, topography, etc.). If more plots were desired while in the field, field crews then selected plot locations using a random compass azimuth to determine direction and the randomly stopped seconds of a stopwatch converted into steps or meters for distance to plot center. Three of the plots were purposefully selected to be near the drone imagery area. I selected sites to ensure a minimum of 45 meters between plots to reduce spatial autocorrelation. For all plots, I navigated to the center of the plot with the help of field crews and recorded the coordinates on a high-resolution Trimble Geo 7X GPS unit. Plot center points were later differentially corrected and post-processed with an average horizontal precision (root mean square error, RMSE) of 0.256 m.

(2) We selected 20 mature trees within and around the UAV study area across a range of damage severities (fully healthy trees to snags) to further supplement comparisons between field data and remote sensing imagery. I also ensured all trees were plainly visible in the canopy when viewed from above and recorded the GPS coordinates for individual trees on the north side of the tree with the receiver against the bark.

The crew recorded the site locality, the date, and plot number if applicable. For both trees within plots and individual trees, the field crew recorded crown class, health status, diameter at breast height (DBH), host species, damage causal agent (DCA) species if possible, and needle color (percent green, gray, or red needles; 5% increments and all three needed to add up to 100%). Crown class historically has been described by level of exposure to light (Smith et al., 1997), but here we estimated tree dominance by evaluating how the upper portion of the tree was positioned relative to other trees nearby (Figure A.2). Dominant trees are the tallest ones in the immediate area. Co-dominant trees are taller than the trees directly next to it, but they are not the tallest in their local cluster. Intermediate trees are shorter than the previous two classes, and only the very top of the tree is visible from above. Suppressed trees have their crowns mostly or completely covered by the foliage of the surrounding trees. Open-grown trees were rare in the study area and describe trees with no immediate neighbors. I grouped tree health status into three broad categories. Healthy trees were mostly green and showed no visible damage, defoliation, or signs of decay. Affected trees are those with some green vegetation remaining but by ocular assessment have been diseased or damaged. Dead trees are those with no green foliage remaining. For trees within plots, crews also recorded tree azimuth and distance from plot center. See Table 2 for explanations of each category and Tables A.1 and A.2 for full field work data. Any variables with an uncertain value were listed as unknown (abbreviated UK).

To assess overall forest health and composition, I calculated (1) the distribution of green needles percentage compared across species, (2) DBH as a function of general tree health (alive, affected, or dead), (3) percentage of trees with greater than 20% red needles, and (4) percentage of trees with visible topkill, with their upper crowns having lost some or all of their foliage. Topkill can be an indicator of stress, disease, or general poor health (Alfaro, 1986) in tree

species. After returning from the field, recorded GPS coordinates and field data are used to find a specific tree, either an individual tree or one within a plot, on UAV data imagery (see following section). I compared field data on tree health to on-screen assessment of UAV imagery to determine accuracy and ability to corroborate the two sets of data. This is done by calculating overall accuracy as well as a chi-square metric (comparing the observed data to data expected by random chance).

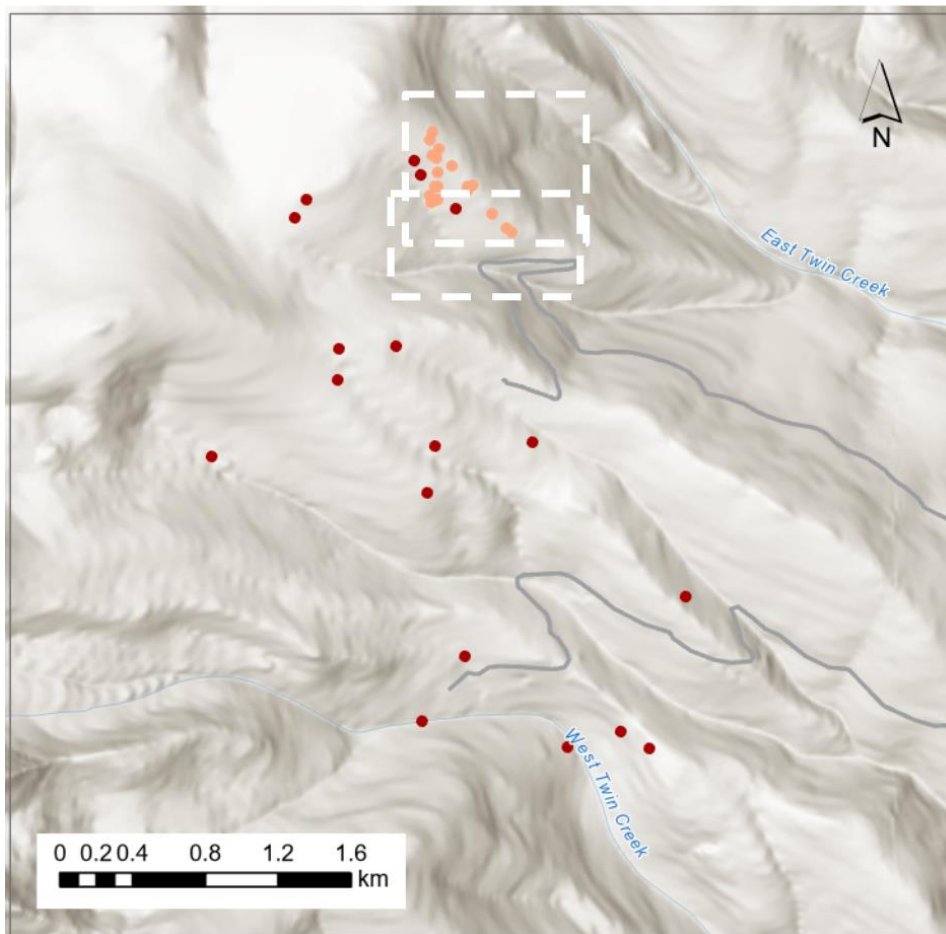


Figure 3. Locations of eighteen 200 m² circular plots (red points) and twenty individual tree locations (orange points) within the study area. Extents of UAV imagery indicated by dashed lines, base hillshade image from ArcGIS Pro.

Table 2. List of measurements taken at sample sites, along with their description.

Measurement	Description
Status	Health of the tree, options of AL (alive), AF (affected, i.e., tree visibly damaged or diseased), or DE (dead)
Diameter at Breast Height (DBH)	Diameter of tree 1.3 m above the ground on uphill side, measured using DBH tape and recorded to the nearest tenth of a centimeter
Host Species	Species of the tree in question (record using standard 4-letter abbreviation, e.g., ABGR for grand fir)
Damage Causal Agent (DCA)	Species that appears to be the main cause of damage of mortality for the tree (insect, fungus, etc.)
Percent Green	Percentage of the whole tree that has green (healthy) needles
Percent Red	Percentage of the whole tree that has red (damaged or diseased) needles
Percent Gray	Percentage of the whole tree where needles are missing, where fine branches may remain
Crown Class	Also called dominance class, describes how the tree stands in comparison to the trees around it, choose one from DO (dominant), CO (co-dominant), IN (intermediate), SU (suppressed), or OP (open)
Distance	Horizontal length from the center of the plot to each individual tree measured using laser range finder or standard tape measure, recorded in meters
Azimuth	Compass angle, measured at plot center, in degrees clockwise from north to tree center

UAV Data Collection

A small section of the total study area (see Figure 2) was recorded using an unmanned aerial vehicle (UAV; also called a drone) on 28 June 2022. The UAV used here, a DJI Matrice 210, was equipped with a MicaSense RedEdge-MX multispectral sensor. Two separate drone flights were conducted adjacent to one another, both in an approximately east-west running

ellipse, with Flight 1 to the south of Flight 2. The UAV data was collected within the same three-day span as field data collection. The multispectral sensor used in this study, hereafter referred to as MicaSense, is a passive sensor, i.e., the sensor collects reflected electromagnetic radiation but does not emit energy like lidar or radar. For these UAV flights, the MicaSense sensor recorded in the blue, green, red, red edge, and near-infrared (NIR) regions of the electromagnetic spectrum, with those bands centered at approximately 475, 560, 668, 717, and 842 nanometers respectively (MicaSense, 2020).

The drone pilot was required to always maintain a line-of-sight with the drone and fly at an approximately consistent altitude of 91 m over the forest canopy. Crew members placed 14 total ground control points (GCPs) on the ground prior to UAV liftoff, which were visible for use in post-flight analysis. I recorded the GPS coordinates of the GCPs, and drone imagery was stitched together after collection and adjusted for topographic distortions by aligning the GCPs seen in drone imagery with the coordinates recorded on the ground, using Agisoft Metashape software. After spatial correction and stitching of the imagery, the final spatial resolution was approximately 0.1 m. Subsequently, I cropped the imagery, as data near the edge of the flight path was stretched or distorted such that it would interfere with data analysis. The two UAV flights resulted in two separate usable imagery sets. Flight 1 was centered around 113.771° W, 46.958° N and produced 0.33 km² of coverage, while Flight 2 was centered around 113.771° W, 46.961° N and produced 0.31 km² of coverage.

Satellite Data Collection

Multispectral satellite imagery used in this study was acquired within one month of the field work. The satellites utilized in this project were WorldView-3, Sentinel-2, and Landsat 9,

which all obtain multi-spectral data with bands in the visible and near-infrared regions of the electromagnetic spectrum. In addition to selecting satellite imagery that had acquisition times close to both field and drone data acquisition, I also chose imagery that was mostly free of clouds, if possible.

I obtained WorldView-3 imagery for our area of interest, acquired on 27 July 2022, by a direct data request via our National Aeronautics and Space Administration (NASA) project collaborator. I used the coastal (400 to 450 nm, also known as ocean blue), blue (450 to 510 nm), green (510 to 580 nm), yellow (585 to 625 nm), red (630 to 690 nm), red edge (705 to 745 nm), and two NIR (705 to 745 nm and 770 to 895 nm) bands. I used only these eight multispectral bands in this study, but the instrument also collects a panchromatic band, detecting wavelengths across a larger part of the visible light spectrum, as well as eight shortwave infrared bands. At nadir, where the satellite is directly above the area to be imaged, the sensor has a ground pixel resolution of 1.24 m (MAXAR, 2020). However, the imagery was orthorectified and processed to top-of-atmosphere reflectance through our NASA collaborators using an API for preparing high-resolution satellite data (Neigh et al., 2019) and provided to us at a resampled spatial resolution of 2 m. When specifically tasked, WorldView-3 is able to revisit the same area multiple times in the span of one week, however I only had access to one image close to the UAV and field data observation times.

Sentinel-2 data, acquisition date 27 June 2022, was obtained using the Copernicus Open Access Hub interface from the European Space Agency (ESA; <https://scihub.copernicus.eu/>), with values representing ground reflectance after correcting for atmospheric scattering and absorption (ESA, 2023). This satellite collects data in 10 m, 20 m, and 60 m spatial resolutions, but I opted to use the 10 m pixels in this study. The 10-m resolution Sentinel-2 sensor data is

available in blue, green, red, and NIR bands, centered around approximately 493, 560, 665, and 833 nm, respectively. Since Sentinel-2 has more than one satellite, most land areas on Earth (with the exception of remote islands and the polar regions) are visited approximately every five days.

Landsat 9 data, acquired on 1 July 2022, was retrieved using the EarthExplorer tool from the United States Geological Survey (USGS; <https://earthexplorer.usgs.gov/>), corrected to surface reflectance values by accounting for atmospheric distortion (USGS Landsat Missions). Landsat 9 is the latest in a series of satellites produced as a collaboration between the USGS and NASA. Available 30-m spatial resolution bands by the Landsat 9 Operational Land Imager (OLI) 2 sensor that were used in this analysis are coastal aerosol (430 to 450 nm, shorter wavelength than blue), blue (450 to 510 nm), green (530 to 590 nm), red (640 to 670 nm), and NIR (850 to 880 nm), as well as two shortwave infrared bands (1570 to 1650 and 2110 to 2290 nm). Spectral resolution, spatial resolutions, and acquisition date for all instruments are listed in Table 3.

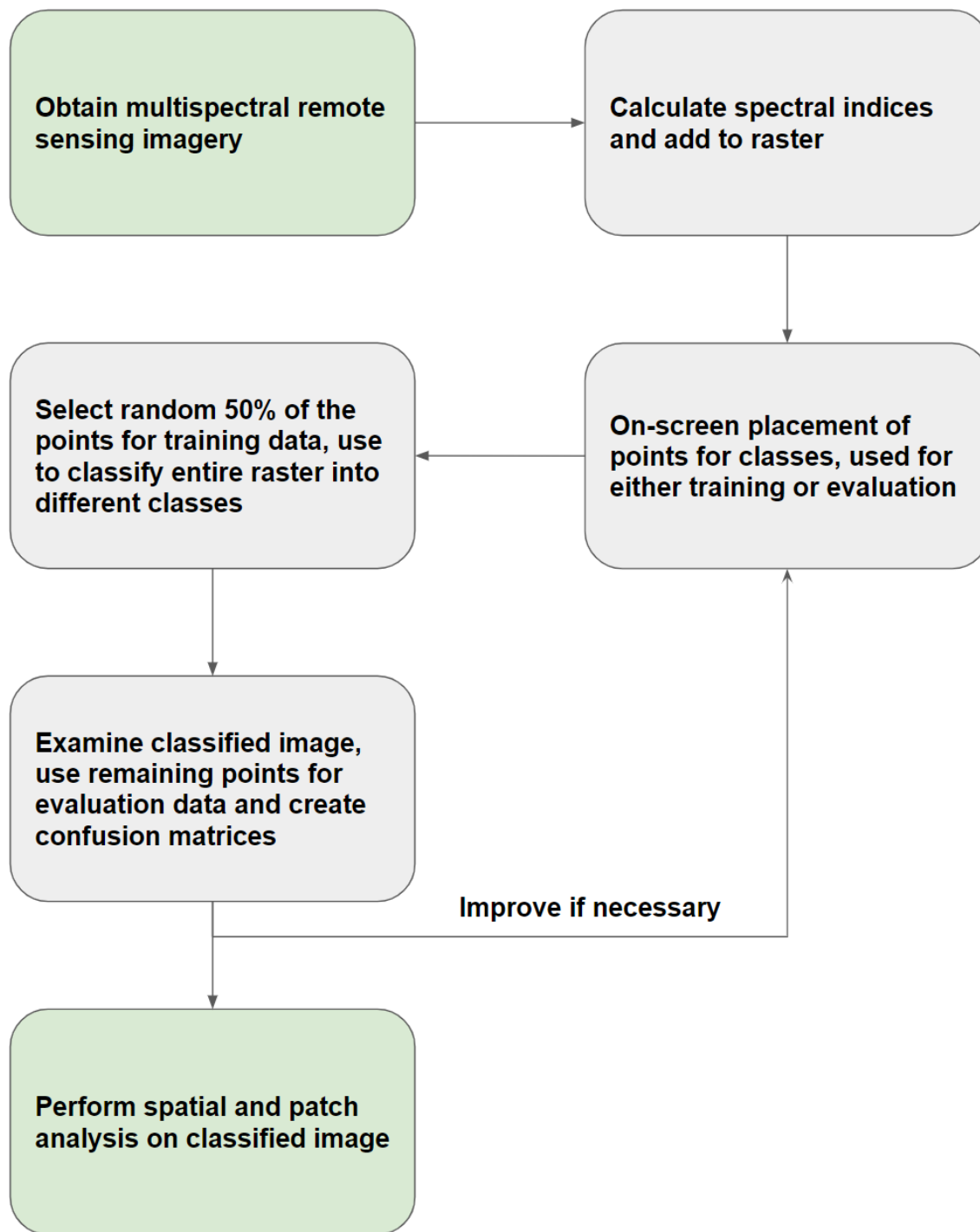


Figure 4. General workflow summary for processing of remote sensing imagery.

Remote Sensing Data Processing

For each satellite or UAV image, I downloaded all imagery from their respective depositories and inspected them separately in ArcGIS Pro 2.9.1 (Esri). The extent of all satellite imagery provided was larger than the study area, so I cropped the pixels to encompass a rectangle that covered the field sites visited, which by default included the UAV data extent. I cropped Sentinel and Landsat satellite imagery to a square area of approximately 25.3 km² centered around 113.77° W, 46.95° N for subsequent evaluation. WorldView-3 data was initially limited to the same extent as above, but some parts of the area contained clouds, reducing the usable area to approximately 20.0 km² once I manually masked pixels of clouds. Reflectance values were displayed in a true color, red-green-blue (RGB) image for initial review and on-screen pixel selection (see Classification Models section). To illustrate the level of detail from each image, trees measured within a plot (and their values for DBH and percent green needles) were compared with imagery of different spatial resolutions.

In addition to the bands provided by the sensors, I also calculated multiple spectral indices and used these as explanatory variables. Spectral indices combine several spectral bands and coefficients into a known equation, which takes advantage of the fact that different substances reflect wavelengths of light at varying intensities, to produce a value that may be more useful than one band alone. In this case, living vegetation reflects elevated levels of NIR light and lower levels of red light, while diseased or dead vegetation has similar NIR and red band reflectance values. In addition, bare soil has high reflectivity across many wavelengths (Jackson & Huete, 1991). I used the following spectral indices when the constituent bands of the indices were available: normalized difference vegetation index (NDVI, Equation 1), normalized difference red edge index (NDRE, Equation 2), enhanced vegetation index (EVI, Equation 3),

and red-green index (RGI, Equation 4). The calculations for the indices used their standard formulas, given below; coefficients for EVI are from the MODIS EVI algorithm (De Petris et al., 2019). Sentinel-2 and Landsat 9 did not have an NDRE value (i.e., only NDVI, EVI and RGI are computed), since no red-edge band is included in the sensors. Additionally, since WorldView-3 contained two near-infrared bands, I calculated two NDVI, two NDRE, and two EVI values each pixel as opposed to just one (Table 3).

Equation 1.
$$NDVI = \frac{NIR-Red}{NIR+Red}$$

Equation 2.
$$NDRE = \frac{NIR-Red\ Edge}{NIR+Red\ Edge}$$

Equation 3.
$$EVI = G \times \frac{NIR-Red}{NIR+C1 \times Red - C2 \times Blue + L}$$

Coefficients: G = 2.5, C1= 6, C2 = 7.5, L = 1

Equation 4.
$$RGI = \frac{Red}{Green}$$

Table 3. Summary of all remote sensing data collected or retrieved. Spatial resolution is at-nadir.

Remote Sensing Instrument	Acquisition Date	Spectral Bands Used	Spectral Indices Used	Spatial Resolution
MicaSense (Unmanned Aerial Vehicle)	28-06-2022	Blue, Green, Red, Red Edge, NIR	NDVI, NDRE, EVI, RGI	~ 0.1 m
WorldView-3 (Satellite)	27-07-2022	Coastal, Blue, Green, Yellow, Red, Red Edge, NIR 1, NIR 2	NDVI 1, NDVI 2, NDRE 1, NDRE 2, EVI 1, EVI 2, RGI	1.24 m (resampled to 2 m)
Sentinel-2 (Satellite)	27-06-2022	Blue, Green, Red, NIR	NDVI, EVI, RGI	10 m
Landsat 9 (Satellite)	01-07-2022	Coastal, Blue, Green, Red, NIR, SWIR 1, SWIR 2	NDVI, EVI, RGI	30 m

Classification Models

To detect insect disturbance in the imagery, I manually inspected each remotely sensed image (MicaSense, WorldView-3, Sentinel-2, and Landsat 9) for visual evidence of tree mortality or defoliation events. Using on-screen interpretation, I placed 80 points in each of the following classes: unhealthy trees (trees with red needles, trees with no needles (gray trees), or a combination; also including dead trees), green trees (trees with green foliage, no distinct red or gray patches), herbaceous plants (low vegetation, less than 1.5 meters, shorter than trees including shrubs), bare ground (no vegetation present), and shadow (light blocked by clouds, vegetation, or topography). Note that I initially separated red and grey tree classes, but then combined these classes due to the similar appearance of the two classes, especially in coarser-

resolution imagery. Defoliators typically do not cause simple green-to-red coloration change of foliage (Senf et al., 2015) as a result of an infestation, and it proved difficult to determine whether loss of needles was from defoliation or gray-stage attack at coarse scales. Therefore, I used these final five classes in land cover classification maps produced in this study. Higher-resolution sensors include individual tree shadows, while lower-resolution imagery has distinct shadows only from clouds and terrain.

Following the selection of pixel locations for each class, I extracted raster cell values (with all applicable multispectral bands and indices listed above) using the points in each image. I randomly split the pixel classes evenly into a training and evaluation dataset. I used 50% of the randomly selected locations for training data ($n = 40$ per class) and the other half (50%) for validation data ($n = 40$ per class). The latter dataset was used to evaluate the accuracy of the image classifications.

I then used the training data as an input for a supervised classification algorithm to predict the land class of each pixel based on all the spectral bands and indices. Supervised classification uses pre-selected points of known values to generate a land classification map for a much larger area (Sisodia et al., 2014). In this case, these points are used to generate a model, which is then applied to a map for land cover class map across the whole area of interest (note that for the MicaSense imagery this total area is much smaller). I classified Landsat 9 imagery with assistance from higher resolution satellite data, as on-screen selection of classes at this resolution is exceedingly difficult if not impossible without other references.

The classification models used in this study are (1) random forest (Breiman, 2001) and (2) maximum likelihood (Sisodia et al., 2014). (1) Random forest is a nonparametric model and uses bootstrapped samples (selections with replacement) and a multitude of decision trees to split

data successively into smaller and smaller groups (Fox et al., 2017). Random forests can be adjusted based on data available for processing and trees used, but the models appear to be robust to error even when the number of variables is increased (Breiman, 2001). In this case, I ran random forest in classification mode and used 500 trees in each model run; the final prediction (i.e., what class each pixel was eventually labeled) from the model was based on majority voting across the trees. I also evaluated the relative importance of each individual variable (band or index) using a separate random forest run using a different, built-in function of ArcGIS Pro. Variable importance may be developed through numerous methods (Belgiu & Drăguț, 2016), but this method uses a Gini coefficient, incorporating how often a variable is used to split a tree as well as the number of trees (Immitzer et al., 2012). Variable importance shows how crucial a band or index is in obtaining an accurate classification. This technique splits the data between training and evaluation using all input points, and thus does not guarantee equal numbers of classes in each array.

(2) For maximum likelihood, a parametric model, the classifier determines the most likely category that a pixel would belong by matching the specific point data to the training data, assuming a normal distribution of probability across each spectral band and index intensity range (Sisodia et al., 2014). In addition to running the model with all available bands and indices, I conducted several test model runs, this time using the same training points but only the five most important bands or indices were incorporated into the model. The top five spectral inputs were determined using the five highest variable importance values derived from random forest modeling described above. These separate runs were conducted to assess and potential correct for multicollinearity issues that can cause classification and accuracy problems in maximum

likelihood models. The maximum likelihood models are consistent in predicting the most likely data match, given baseline assumptions on normality are achieved (Kiefer & Wolfowitz, 1956).

I repeated the process of producing land classification maps and evaluating the outputs by visual assessment, adding, or changing training points to account for significant misclassification as necessary (Figure 4). The two flights of the UAV imagery are both trained and classified separately, since there were two distinct swaths of coverage. In each case, I compared the produced map to the withheld evaluation data points and then produced quantitative measures of accuracy via confusion matrices. Producer's accuracy is a measure of how many pixels had their actual and predicted class match out of the total number of pixels known to belong to one class ("ground truth" points despite being on-screen selections), while user's accuracy describes how many pixels had matching actual and predicted class values out of all pixels in one predicted category ("predicted" points). I also calculated overall accuracy, which is the percentage of pixels that have their class correctly predicted out of the total number of evaluation pixels (in this case 200 pixels).

Spatial Detection Analysis

Once a map of land cover classes was produced, I produced statistics based on spatial properties and model classifications to provide a summary of each model run. The measures used in this study focused on the unhealthy tree class only and were: (1) the percentage of unhealthy tree pixels from the total number of tree pixels (unhealthy trees plus green trees), (2) percentage of unhealthy trees out of total area, (3) percentage of unhealthy tree subpixels within larger unhealthy tree superpixels compared to the predicted class of those superpixels. These metrics were computed via ArcGIS Pro as well as RStudio for R 1.4.1717 (R Core Team, 2021).

The percentage of pixels, either out of only forest-classified pixels or the whole area of interest, that are classified as unhealthy trees provides an indication of how the different spatial resolutions compare in ability to detect disturbance (i.e., detection sensitivity), and is used here to test metrics on empirical data, as suggested by Frohn & Hao (2006). Overall percentage of affected trees should remain constant if all models and resolutions have equal predictive power for affected trees. However, differences in the overall proportion of unhealthy trees may indicate errors of over- or underestimation for the different spatial resolutions and indicate how sensors can be used for detection of tree disturbance events.

In order to assess errors of omission when detecting dispersed mortality (i.e., underestimation) versus errors of commissions when detecting clustered or severe mortality partially covering a pixel at coarse resolutions (i.e., overestimation), the WorldView-3 and Sentinel-2 pixels were separately aggregated into pixels that match the resolution of coarser imagery. For example, all approximately 2 m pixels within a 30 m by 30 m area were combined into one coarser resolution pixel (hereafter referred to as a superpixel) of 30 m by 30 m after ensuring pixel collocation between rasters, with its value the proportion of unhealthy tree pixels of the finer resolution (hereafter referred to as subpixels), in this case the classified 2-m pixels. I then compared the superpixels to which class was assigned to them via the random forest modeling (the most accurate classification algorithm). Pixel dimensions used here refer to spatial resolution of the sensor at nadir, but may vary due to imagery capture and projection changes. I separated the disturbance severity levels into bins (>0 to 10%, >10% to 20%, >20 to 30%, etc.), by subpixel unhealthy tree percentage, and then I determined the classified superpixel land class frequency for each bin. In other words, each superpixel is assigned two values: a categorical class value from the random forest model run at the superpixel's native (original) resolution and

a quantitative value equal to the percentage of unhealthy tree subpixels within it, determined by the random forest model run of those subpixels. Importantly, for the above analysis, the shadow class was removed for all calculations. Additionally, a window analysis was conducted on the Sentinel-2 and Landsat 9 classification maps, with the percentage of unhealthy tree pixels plotted for both sensors within a moving 250 m by 250 m area. MicaSense-sized pixels were also aggregated into superpixels of sizes corresponding to WorldView-3, Sentinel-2, and Landsat 9 for visualization and distribution analysis.

RESULTS

Field Observations

Trees at the Missoula site, including single trees and trees within plots, had an average DBH of 17.9 cm, with the largest DBH recorded at 63.7 cm. Across the study area, I observed trees that were 100 percent green as well as trees that were 100 percent gray, however the highest percentage of red needles recorded on an individual tree was only 80 percent (i.e., there were no fully red trees). Many trees were likely killed several years prior to the field visit, and I determined that the main disturbance agents were most likely western spruce budworm (for topkill) and mountain pine beetle (for older dead, gray trees), although in-field determination of the exact disturbance agent was not readily evident. When trees in the field were compared to those in UAV imagery, there is a 75% overall accuracy rate matching healthy or unhealthy and dead trees between the two data sets (Table 4); however, there is low sample size ($n = 12$) and derivation from random chance is not highly significant ($\chi^2 = 3.086$, $p = 0.0789$).

The remaining analysis of the field data focused on the trees measured within plots. I noted that these trees measured in the plots exhibiting various levels of decline based on species, with subalpine fir showing the lowest mean percentage of green needles with plot trees averaging 33.7% green needles (Figure 5, median values shown). DBH values did not vary significantly between health classes of alive, affected, and dead trees within plots (one-way ANOVA, $p = 0.454$) (Figure 6). Additional noteworthy conditions include that only five trees (1.8%) were recorded with red needles of 20% or more of in their canopies, and 30 trees out of a total of 276 trees recorded (10.9%) had visible topkill.

At the approximately 0.1 m resolution of MicaSense, individual trees were still visible in imagery and therefore could be compared directly to the trees measured in the field (Figure 7).

The tree locations were in the correct positions, and trees without fully green crowns in MicaSense imagery were marked as being affected or dead in the field.

Table 4. Comparing the health of trees as recorded in the field versus how the tree appears on-screen for UAV data after collection.

	Field Assessment	
UAV On-Screen Assessment	Healthy Tree	Unhealthy or Dead Tree
Healthy Tree	5	2
Unhealthy or Dead Tree	1	4

Overall Accuracy = 75%
 $\chi^2 = 3.086, p = 0.0789$

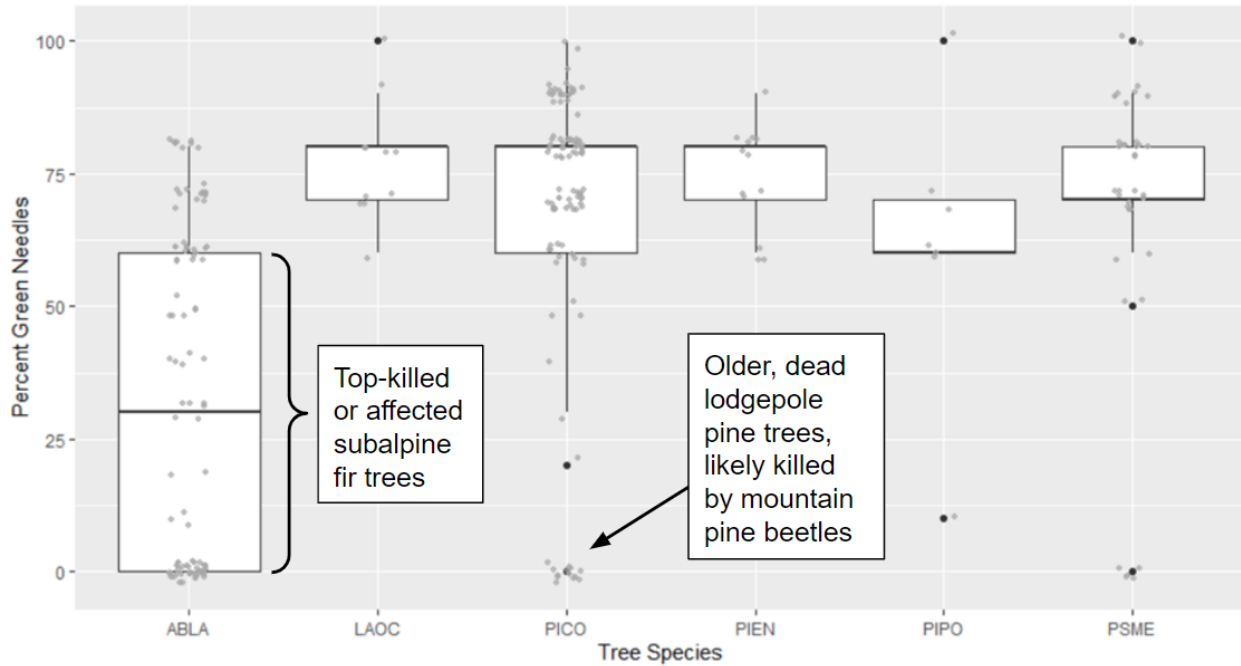


Figure 5. Percentage of green needles for each tree as a function of tree species (PICO = lodgepole pine, ABLA = subalpine fir, PIEN = Engelmann spruce, PSME = Douglas-fir, PIPO = ponderosa pine, LAOC = Western larch). Gray points are single tree values, black points indicate value of one or more outliers. Notable patterns listed.

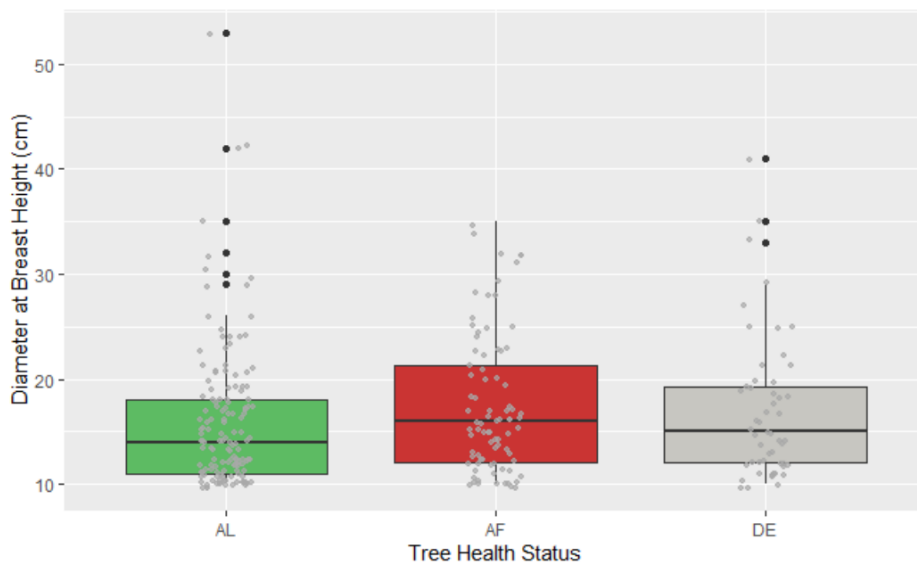


Figure 6. Diameter at breast height (DBH, cm) as a function of tree health status (AL = alive, AF = affected, DE = dead). Gray points are single tree values, black points indicate value of one or more outliers. No significant differences between health statuses (one-way ANOVA, $p = 0.454$)

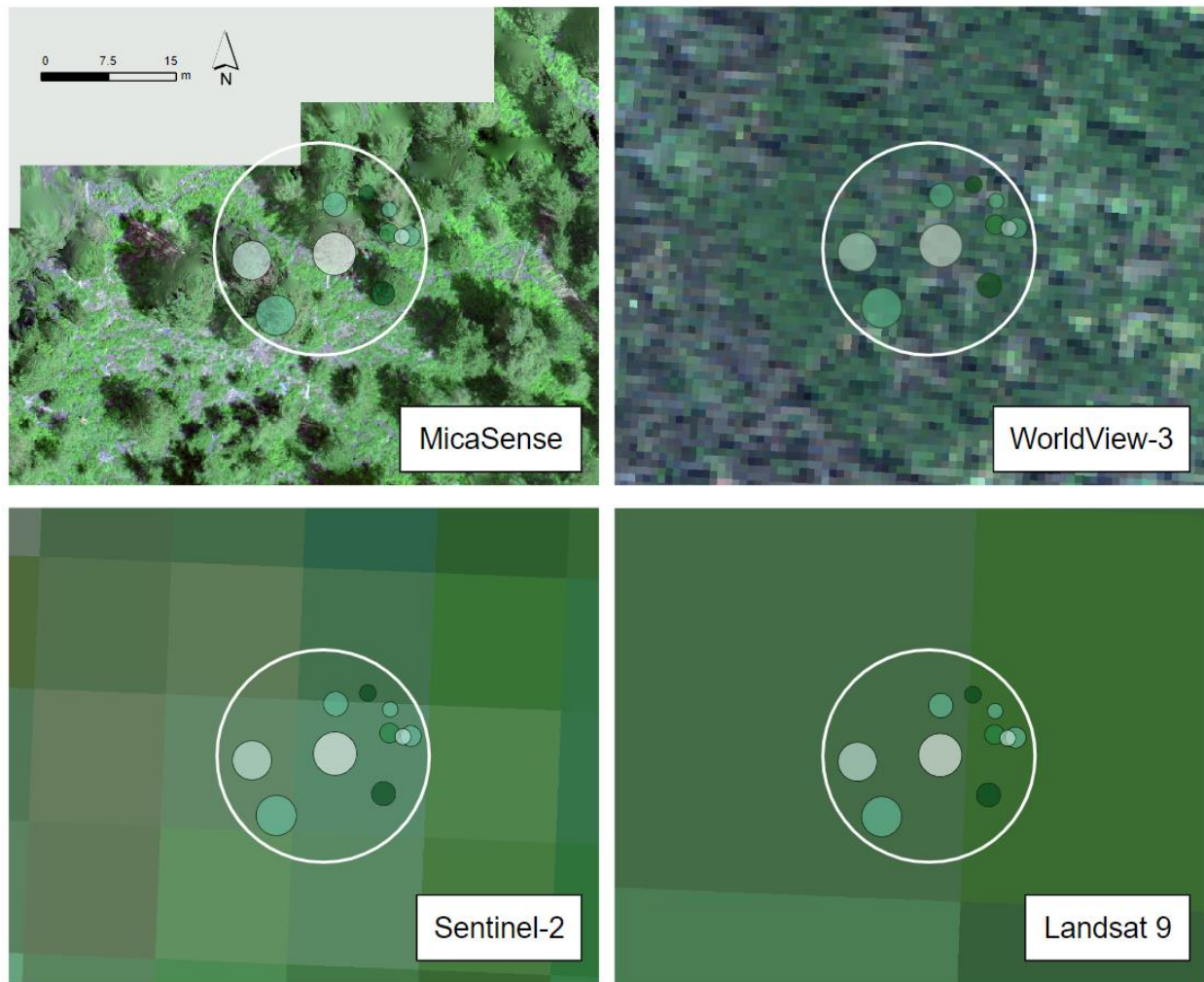


Figure 7. Overlay of one plot of trees recorded in the field (large white circle shows approximate 8-meter fixed-radius plot boundaries) with RGB imagery of different resolutions (background raster labeled, WorldView-3 (©2022, Maxar, USG Plus) not co-located with plot due to clouds). Small, green-filled circles inside of plot indicate individual trees, with circle size indicating DBH, to scale between trees but not to the base image, and green gradient color indicating percentage of green needles on tree, from 50% (white) to 90% (dark green).

Classification Models

I produced classification maps for MicaSense Flight 1, MicaSense Flight 2, WorldView-3, Sentinel-2, and Landsat 9 each using both a random forest and maximum likelihood classifying model (Figures 8 and 9). Tests of maximum likelihood models with limited variables produced lower overall accuracy than the same models but with full variable selection. These models will not be discussed further. The random forest models consistently had a higher overall accuracy than their corresponding maximum likelihood model at the same resolution (84.5% to 81.5% for MicaSense Flight 1, 81.5% to 80% for MicaSense Flight 2, 94.5% to 92% for WorldView-3, 94.5% to 91% for Sentinel-2, and 97.5% to 96.5% for Landsat 9, so random forest results will be the focus here. The random forest model, when used on the evaluation data of MicaSense Flight 1 imagery, had an overall accuracy of 84.5%. For the random forest classification of MicaSense Flight 1, the highest producer's accuracy, the probability of a reference pixel being correctly classified, was shadow (100%). The class with the highest user's accuracy, the probability of the classified pixel actually representing that class, was also the shadow class (97.56%) followed by unhealthy trees (97.14%). For MicaSense Flight 2, random forest modeling produced an overall accuracy of 81.5%. The highest producer's accuracy was shadow (95%) followed by unhealthy trees (90%). The class with the highest user's accuracy was shadow (92.68%) followed by bare ground (91.89%). See Tables A.3 to A.7 for details.

Random forest modeling of WorldView-3 imagery produced an overall accuracy of 94.5%. The highest producer's accuracies, all tied at 97.5%, were bare ground, herbaceous, and shadow classes. The class with the highest user's accuracy was shadow (97.5%), followed by unhealthy trees (92.7%). Random forest modeling of Sentinel-2 imagery also produced an overall accuracy of 94.5%. The highest producer's accuracy was the herbaceous class (97.5%).

The classes with the highest user's accuracies were green trees and shadow (both 100%). After processing Landsat 9 data, the random forest model had an overall accuracy of 97.5%. The herbaceous class had the highest producer's accuracy (100%), while bare ground had the highest user's accuracy (100%). See Figure 10 for a visual summary of accuracy data.

The most important variables, as determined by random forest modeling, were NDVI, NDRE, and NIR for both MicaSense flights (Figure 11). WorldView-3 has NIR, red edge, and blue bands as having the highest relative importance. The most important bands for Sentinel-2 are green, blue, and NIR, while for Landsat 9 the top three variables are EVI followed by RGI and the SWIR 1 band.

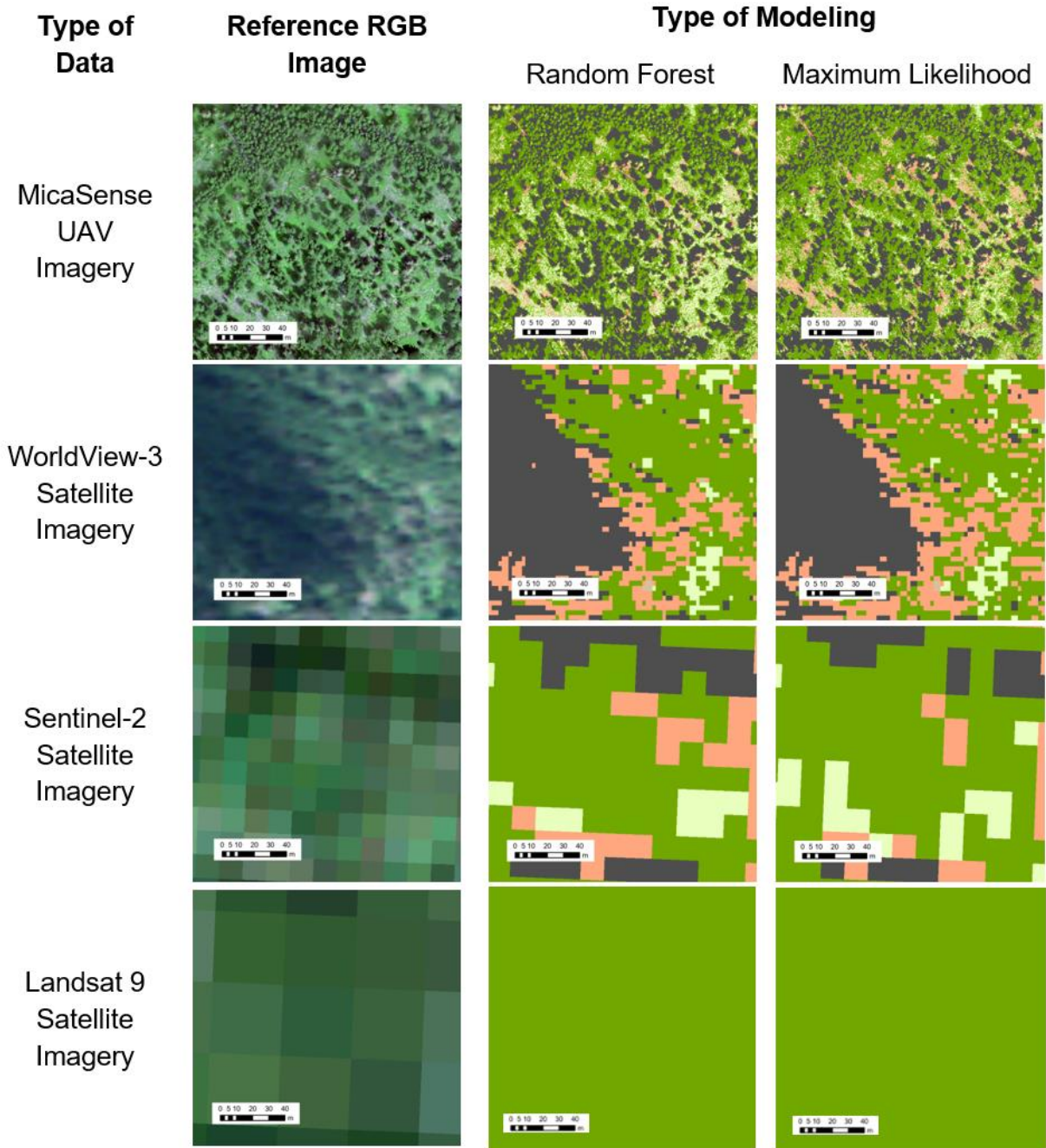


Figure 8. Comparison of image classification for one location of approximately 0.03 km² in area, using either random forest or maximum likelihood modeling, with an RGB image for reference.



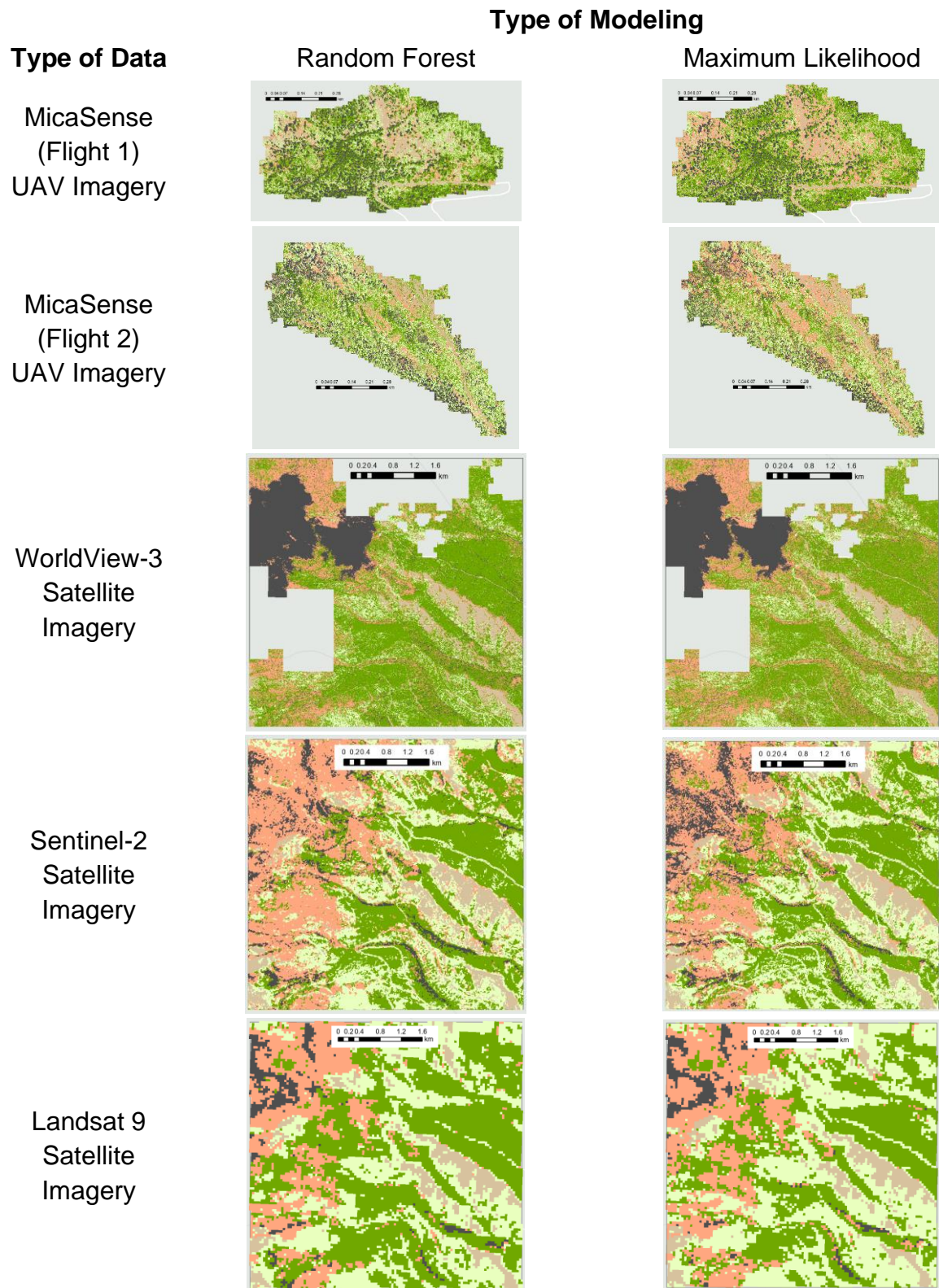


Figure 9. Classifications of the sensors used at the fullest extent possible for each image; legend same as Figure 8.

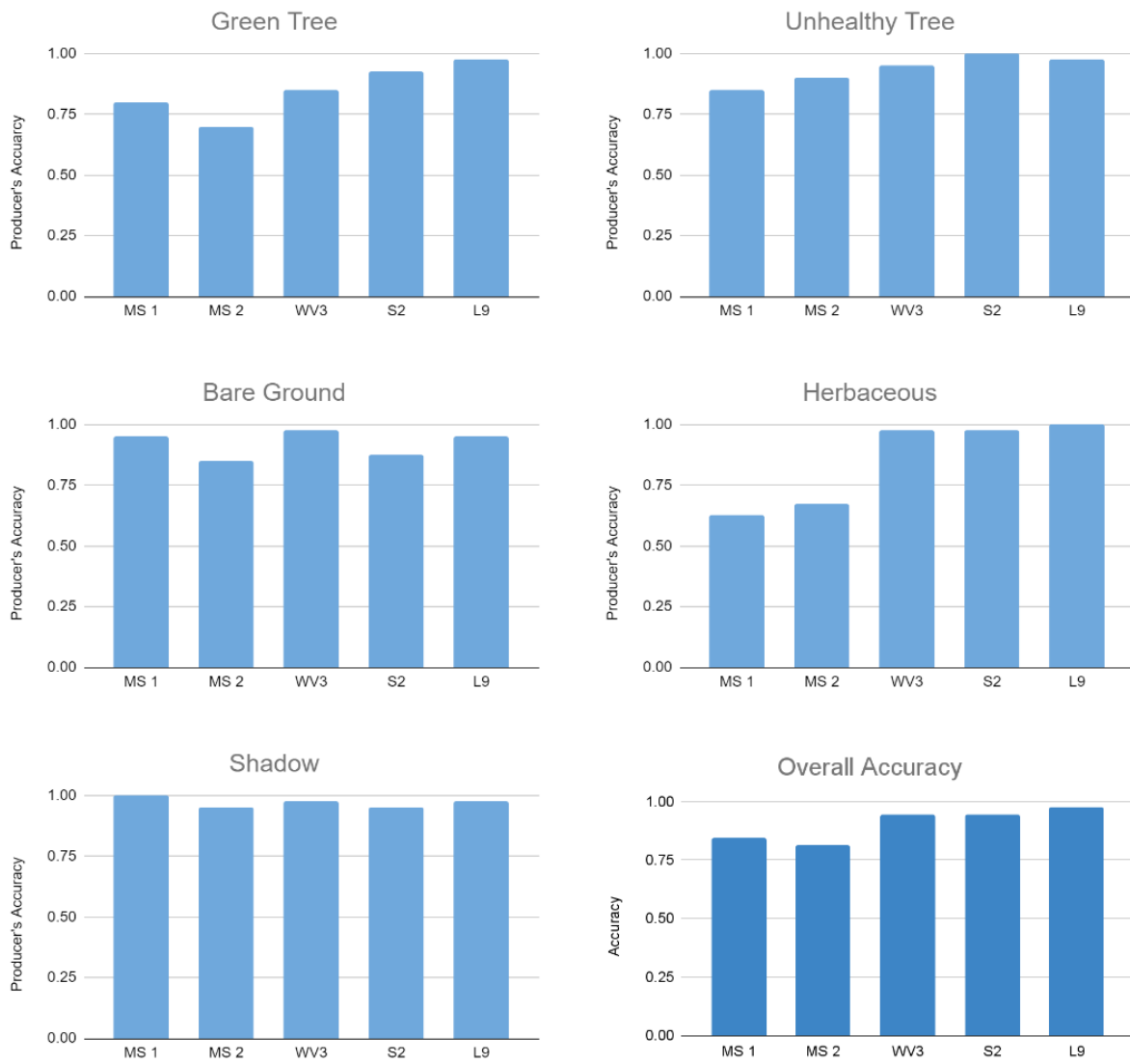


Figure 10. Comparison of the random forest producer's accuracy for the five different classes (each panel labeled) and the overall accuracy across remote sensing devices: MicaSense Flight 1 (MS 1), MicaSense Flight 2 (MS 2), WorldView-3 (WV3), Sentinel-2 (S2), and Landsat 9 (L9).

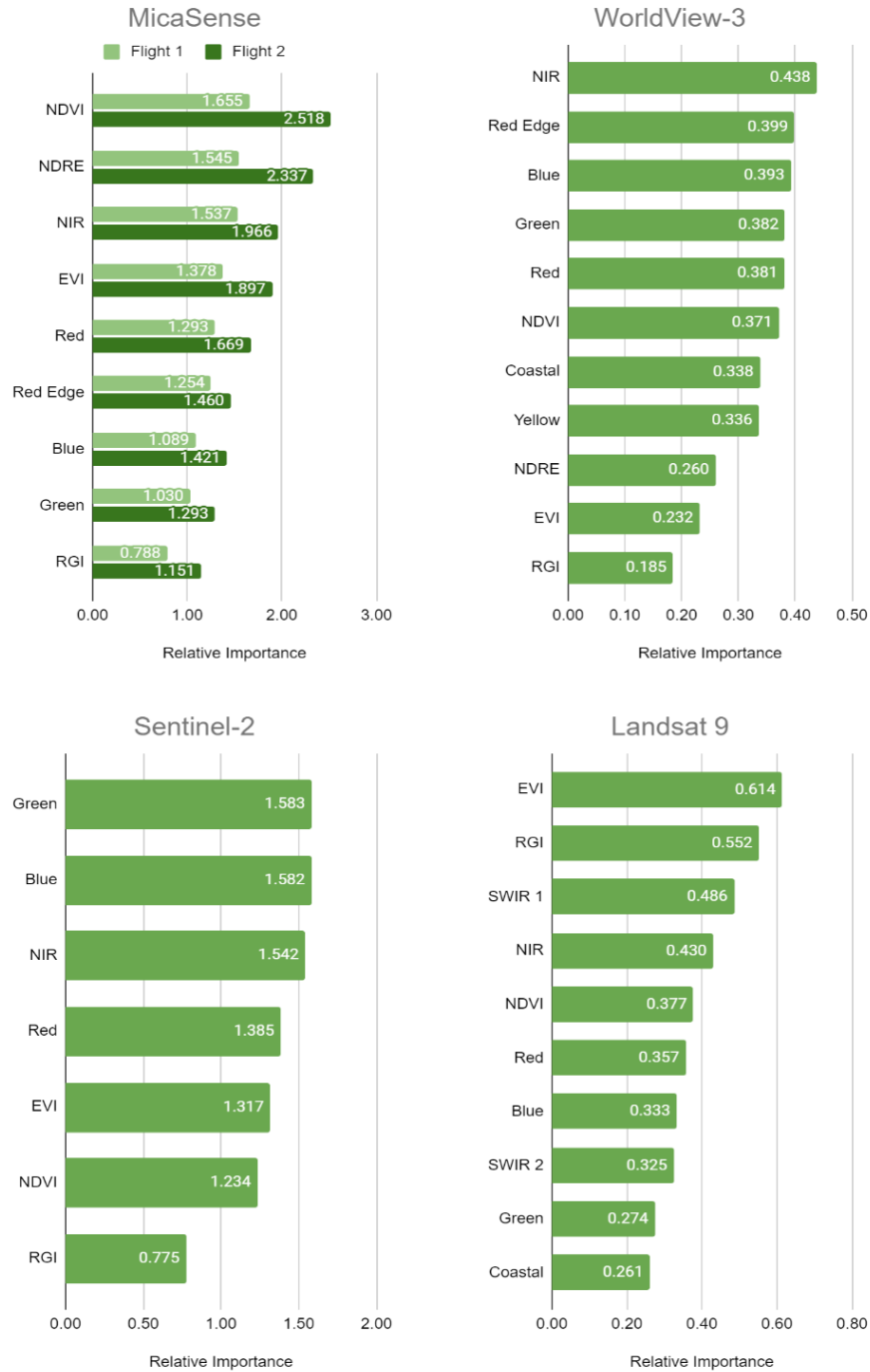


Figure 11. Gini relative variable for applicable spectral bands and indices from a random forest classification across remote sensing devices. Spectral bands abbreviated for near-infrared (NIR) and shortwave infrared (SWIR 1 and 2). Spectral indices are normalized difference vegetation index (NDVI), normalized difference red edge (NDRE), enhanced vegetation index (EVI), and red-green index (RGI). WorldView-3 has two NIR bands and thus has two NDVI, NDRE, and EVI values (each averaged into one value shown here).

Spatial Detection Analysis

At these coarser resolution pixels, a single pixel may consist of multiple trees, yet unhealthy tree pixels were hypothesized to need to contain at least a majority red or gray trees in order to be able to correctly classify the pixel as the unhealthy tree class. In areas where tree damage was occurring at moderate and dispersed levels as evident from the MicaSense imagery (Figure 8, top panel), Landsat 9 pixels were classified entirely as healthy trees (Figure 8, bottom panel), seemingly indicating an underestimation of tree disturbance detection in coarser-level imagery for dispersed damage.

When aggregating the MicaSense image classification to coarser superpixels, the variability in unhealthy tree percentage within superpixels decreased. Aggregated superpixels went from containing anywhere from 0% to well over 80% unhealthy tree MicaSense subpixels (for WorldView-3 superpixels) to all superpixels containing less than 40% unhealthy tree subpixels (for Landsat 9 superpixels) (Figure 12). All three sensors had their distribution of percentage of unhealthy tree subpixels within superpixels highly skewed to the right (Figure 12). Additionally, when analyzing the aggregated WorldView-3 classification, after removing null values and the shadow class, a higher proportion of unhealthy trees corresponded with an increased likelihood of that pixel being classified as unhealthy trees in the coarser resolution imagery. However, there were no bin of subpixel disturbance that exhibited either a 0% or 100% frequency of unhealthy tree class superpixels (Figures 13 and 14), and all other superpixel classes remain across all subpixel percentage groups. When analyzing the expected mortality from WorldView-3 for the coarser resolution Landsat and Sentinel superpixels once the shadow class was removed, six subpixel disturbance bins corresponded to fewer than expected unhealthy trees at the Sentinel-2 resolution, while five bins were linked to less disturbance at the Landsat 9

resolution (Figure 15). No subpixels groups corresponded to a greater frequency of unhealthy trees than expected for Landsat 9 superpixels, although superpixel unhealthy tree class frequency was on the high end of the range of values indicated by subpixels at the >80% to 90% subpixel group. Sentinel-2 superpixel best matched their subpixel groups from 10% to 40% subpixel disturbance (i.e., the frequency of unhealthy tree-classified superpixels was within the range to match the percentage of unhealthy tree-classified subpixels within them). Sentinel-2 consistently, but not always, had a higher percentage of unhealthy tree pixels than Landsat 9 when evaluated within a 250 m by 250 m moving window (Figure 16)

When evaluating landscape patterns of red or gray trees, the percentage of unhealthy tree pixels within the forest classifications of satellite sensors ranged from 24.3% to 47.2% (Figure 17). When restricted to UAV study areas, percentage of unhealthy tree pixels out of total tree pixels ranges from 0% for Landsat 9 pixels within MicaSense Flight 1 to 46.5% for WorldView-3 pixels within MicaSense Flight 2.

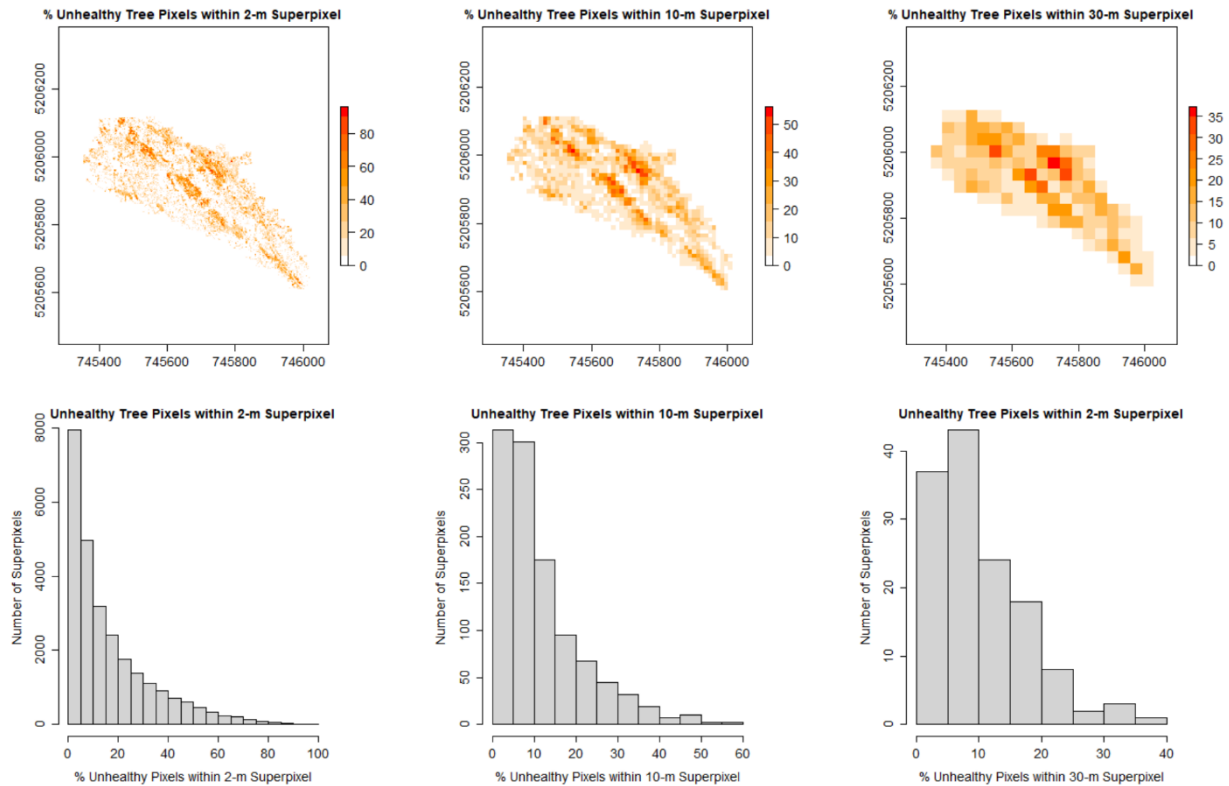


Figure 12. Percentage of MicaSense pixels classified as unhealthy trees within a superpixel of WorldView-3 (2 m, left panels), Sentinel-2 (10 m, middle panels), and Landsat 9 (30 m, right panels) size as a map (top row) and histogram (bottom row).

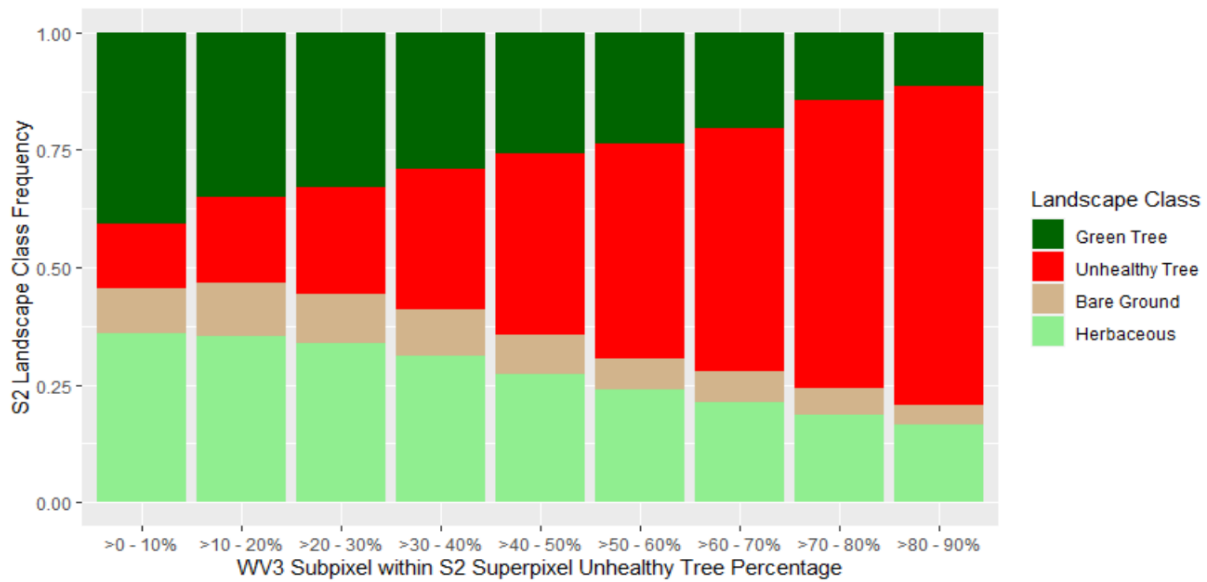


Figure 13. Comparison between random forest-classified Sentinel-2 superpixels and the constituent frequency of unhealthy tree classification of WorldView-3 subpixels.

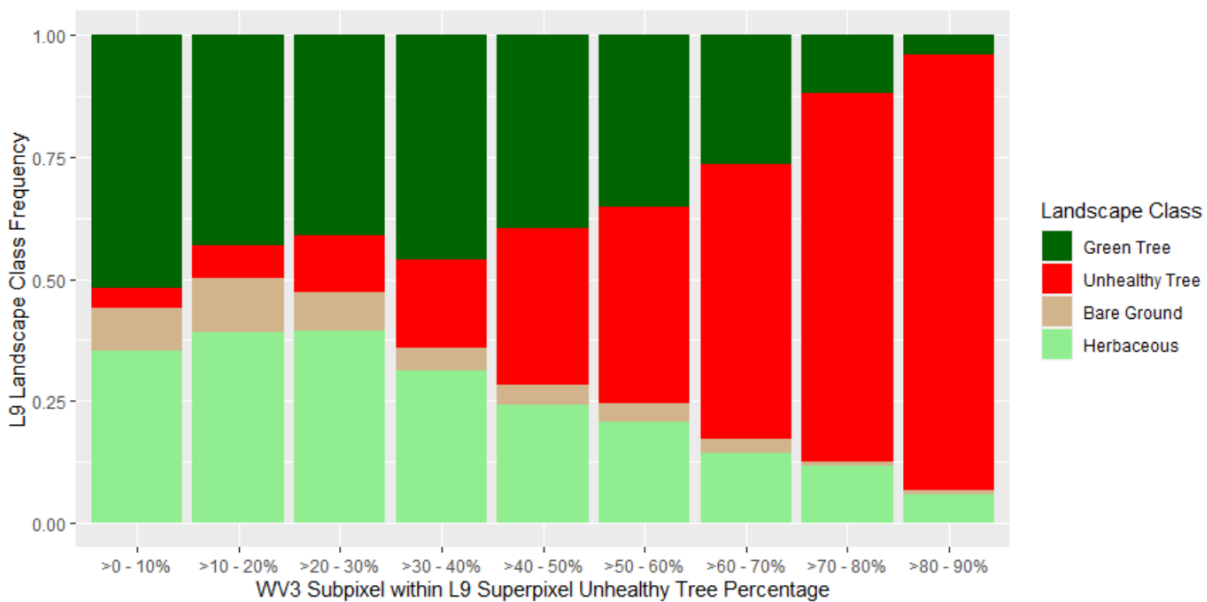


Figure 14. Comparison between random forest-classified Landsat-9 superpixels and the constituent frequency of unhealthy tree classification of WorldView-3 subpixels.

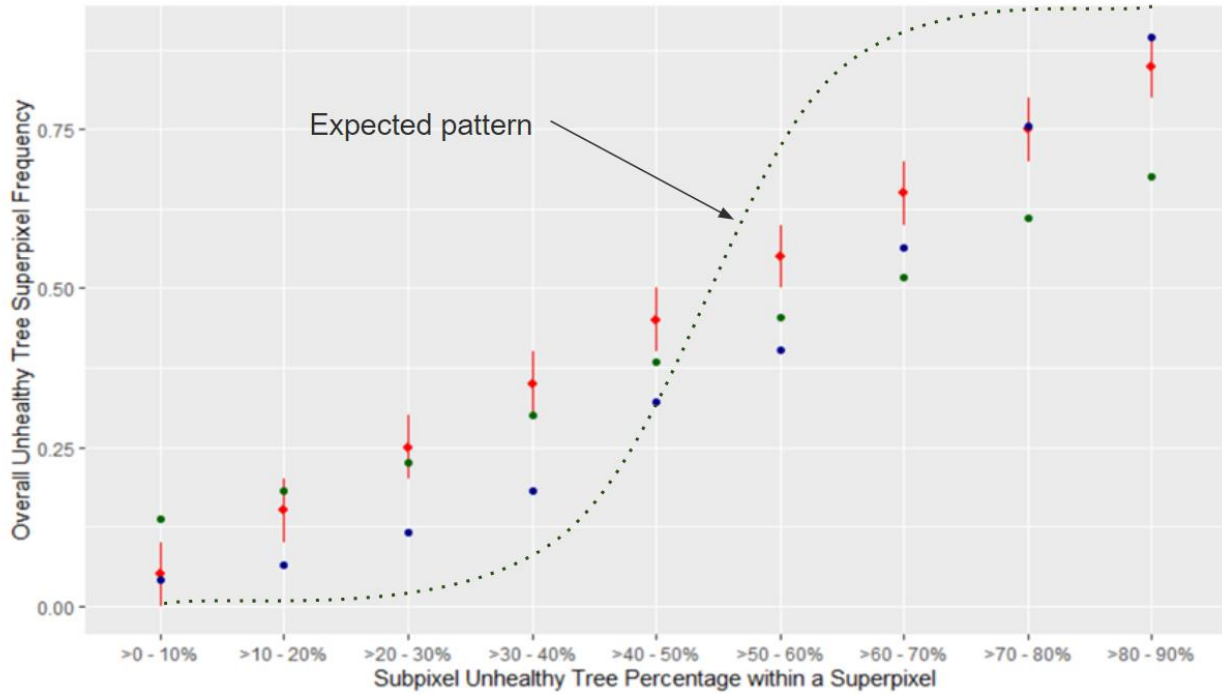


Figure 15. Comparison of Sentinel-2 and Landsat 9 superpixels, plotted by their frequencies of WorldView-3 subpixel disturbance (in groups of 10 percentage points) and frequencies of unhealthy tree superpixel classification; red lines are equality lines (subpixel classification percentages match superpixel classification frequency); dashed line expected trend.

- Sentinel-2 Superpixels
- Landsat 9 Superpixels
- Subpixel to Superpixel Equality Lines

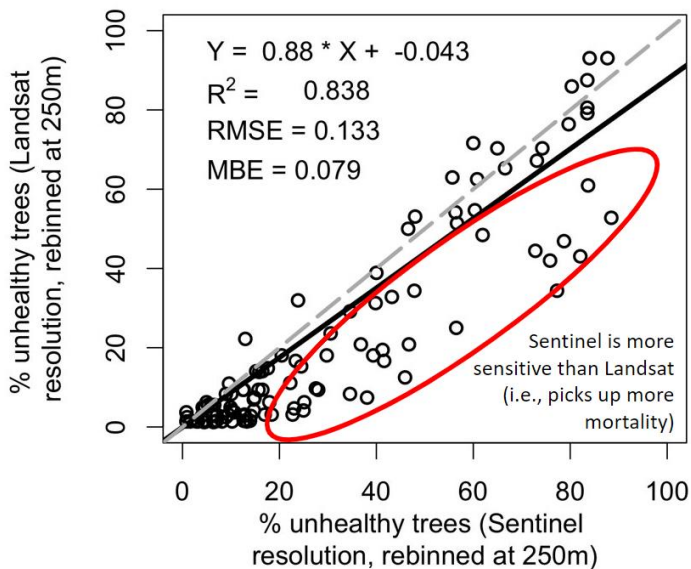


Figure 16. Comparing percentage of unhealthy trees for Landsat 9 and Sentinel-2 within a 250 m by 250 m moving window.

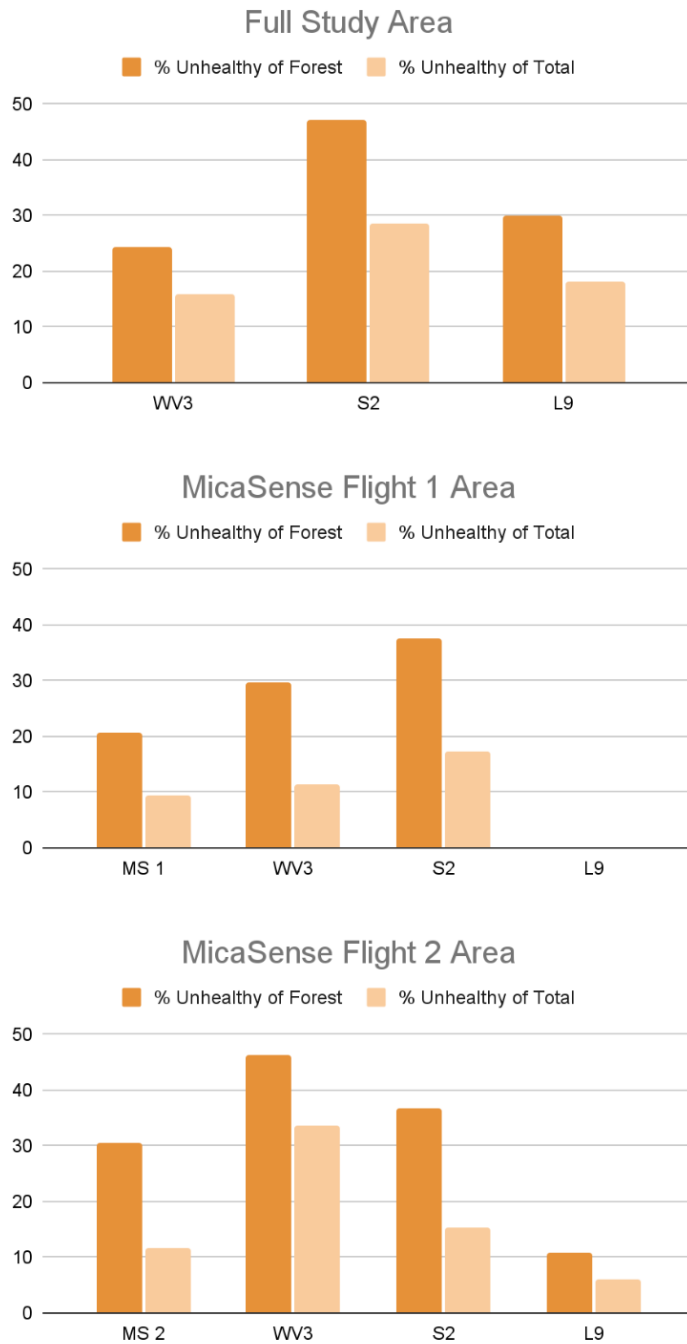


Figure 17. Total unhealthy tree patch percentage values (both out of forest pixels and total pixels) for MicaSense Flight 1 (MS 1), MicaSense Flight 2 (MS 2), WorldView-3 (WV3), Sentinel-2 (S2), and Landsat 9 (L9) after running a random forest classification model. Analyzed for full study area (top), as well as MicaSense Flights 1 (middle) and 2 (bottom).

DISCUSSION

I successfully used an on-screen selection process for classifying UAV and satellite imagery data that encompasses insect damage across various spatial resolutions and scales to analyze detection patterns and processes of a forest host to several insect-caused disturbances.

Field Work

Subalpine fir trees did, on average, have substantial fewer green needles than other trees in the study area. Subalpine fir is a primary host for both balsam woolly adelgid as well as western spruce budworm (USFS Field Insect Guides; <https://www.fs.usda.gov/foresthealth/publications/fidls/index.shtml>), and thus may be the cause of this particular disturbance. Ponderosa pine had the second lowest median percentage of green needles, although the variability was large. After over a decade since the recorded outbreak of mountain pine beetle (USFS, R1 All Years IDS Data, <https://www.fs.usda.gov/foresthealth/applied-sciences/mapping-reporting/detection-surveys.shtml>), many pines will likely have fallen over and thus not recorded or have regrown but not to maturity yet. The older the outbreak of insects, the more difficult it may be to accurately identify a damage causal agent. Health was not affected by DBH, possibly indicating that tree age is not a key factor in increasing the baseline stressors of the forest.

UAV Imagery

MicaSense UAV imagery was able to resolve incredibly fine details that no other sensor in this study was able to capture, including trees with topkill and individual tree crowns. However, the very small pixel size leads to an increase in the possibility of excessive

heterogeneity when picking training points on screen. There is a marked decline in overall and producer's accuracy, particular to herbaceous and green tree classes, which may be due to this variability. In addition to capturing detail within individual tree crowns, such as topkill, a notable feature of defoliators (Alfaro, 1986), the UAV flights were also able to distinguish large, down woody debris on the forest floor, something that is not possible with the coarser resolution imagery in this study. Even the finest resolution satellites cannot capture details within tree crown dynamics either (Figure 10), such as differences in reflectance values within a single tree crown (Coops et al., 2003). Although not within the main scope of this research, it is important to note that corroboration was less easily ascertainable at the approximately 2-meter resolution of WorldView-3. Sentinel-2 and Landsat 9 no longer show the detail of individual trees, and groups of trees are captured in a single pixel (Figure 7).

Satellite Imagery

WorldView-3 imagery was still able to identify individual crowns of trees in certain cases, but this level of detail was mostly lost when converting to a classified image. There was better success in terms of overall accuracy when evaluating the random forest modeling technique, at 94.5% overall accuracy, which was the exact same value as Sentinel-2. However, I had to contend with significant coverage in the area of both clouds and their associated shadow, which presents an added challenge to those wishing to run analyses close to real-time. Class-based accuracy is high consistently, with a slight decrease in green tree producer's accuracy.

At the Sentinel-2 scale, even broad indicators of landscape type become difficult to distinguish, such as areas of bare ground or low-lying vegetation (Figures 8 and 9). Regions with apparently diseased or dead trees show an oversaturation of classified pixels. This can present a

problem in narrowing down the exact locations of forest health issues, instead only being left with a general area. However, even at 10-m resolution, roads and topographic details remain intact. Additionally, the lower number of pixels means easier or faster processing of spatial analysis. Overall, this indicates that imagery such as Sentinel-2 could be used first to identify specific regions of interest for those with concerns in ecosystem productivity or patterns, and then these areas can then be evaluated using higher-resolution data, which is especially useful given the high revisit time of Sentinel-2 (Senf et al., 2017).

Landsat-scale resolution loses any indication of herbaceous plants or unhealthy trees in the small study areas (Figure 8). However, overall accuracy is high, and user's and producer's accuracy remain high across classes. Resolutions similar to Landsat satellites would only be helpful in the broadest of contexts, as 8-meter circular plots taken in the field are reduced down to a single pixel, and distinguishing between different land classes becomes extremely difficult. Therefore, it may only be applicable to use Landsat for relatively large areas of each class or category, or when coupled with multitemporal data (Meigs et al., 2011).

Classification Accuracy and Importance

Random forest (non-parametric) models slightly but consistently outperformed the maximum likelihood (parametric) models (i.e., higher overall accuracy) given the same inputs, which may indicate that the random forest model is more robust for complicated interactions between variables (e.g., including non-linear responses; Evans et al., 2011) as opposed to the maximum likelihood model.

Overall, models were extremely proficient in accurately identifying the classes used in this study, especially at coarser resolutions, and multiple classes had 100% user's or producer's

accuracies. However, trees classified as unhealthy were often classified as bare ground in on-screen selection, although gray trees did not have the absolute lowest user's accuracies (herbaceous class had lowest in four out of five image classifications). Unhealthy trees were not consistently misclassified more than other classes. It may be that a fusion is needed between small footprint lidar analysis and multispectral remote sensing to distinguish features like a snag (Martinuzzi et al., 2009). This may be because once vegetation has become sufficiently desiccated, reflectance occurs at higher intensities across the electromagnetic spectrum, similar to soil and rock. The distinction between green trees and herbaceous plants also presented problems, especially at very coarse resolutions. Classification models showed the importance but also downfall of including a shadow class in assisted classification schemes. Shadow pixels consistently had high user's and producer's accuracies across resolutions. However, in some cases, especially with finer than one-meter pixels, shadows appeared to be overclassified. This presents a problem due to the class "hiding" some information that may still be able to be extracted from a raster image. Looking at previous studies, most analysis on both bark beetles and coniferous defoliators was conducted using medium spatial resolution satellites, with bark beetle studies showing repeated use of high and very high spatial resolutions (Senf et al., 2017). This should be reconsidered for future studies, as the tree dieback and variable mortality patterns may only be detectable on very high-resolution sensors, as shown above.

More broadly, when comparing overall accuracies across resolutions, the higher UAV resolution imagery had lower classification accuracy as compared to coarser imagery (Figure 10). This is similar to the study of Meddens et al., (2011), that found that more detail (higher spatial resolution) may not always result in a better classification raster. This is not a consistent relationship when comparing spatial resolution to producer's accuracy. Herbaceous plants show

a noticeable decline in accuracy at high resolutions while the shadow class has high accuracy values across sensors. This may be due to the spectral heterogeneity of herbaceous plants that only is visible at very fine spatial resolutions (Torres-Sánchez et al., 2015), as stated previously. Unhealthy trees are also viewed differently at different resolutions, with very fine imagery showing both red and gray trees, as well as partially affected trees, while coarse imagery only shows general spectral changes to indicate that a stand contains unhealthy (i.e., non-green) trees. This is also in contrast with detection and classification of the human-built environment, which has previously shown slightly higher accuracy when using UAV data as compared to high-resolution satellite data (Zhou et al., 2018).

Variable importance was not consistent across scales either, with NDVI proving much more useful at very high resolutions. However, using random forest is robust against multiple variable influences (Fox et al., 2017), so this difference may not present much of a problem. Importance of variables, using a random forest model and Gini index, could vary as seen here for several reasons. NDVI was consistently higher ranking amongst the MicaSense imagery analyzed, indicating it still has potential use for insect surveys, although middle to lower importance on coarser-resolution sensors may support previously researched limited predictive power of NDVI specifically (Bergmüller & Vanderwel, 2022).

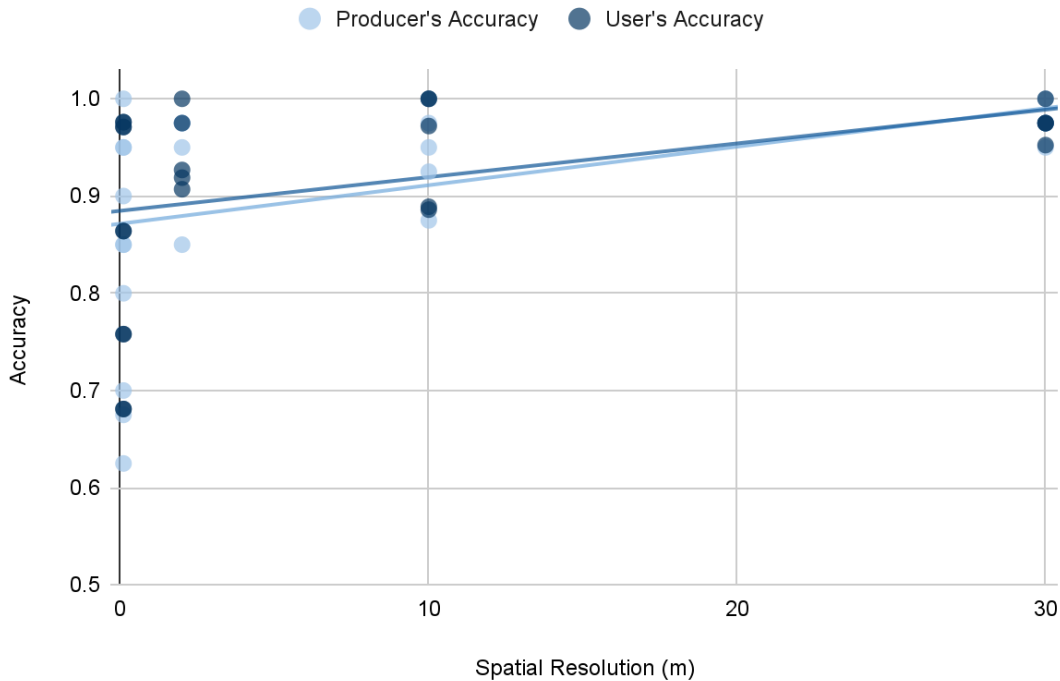


Figure 18. Points from all model runs comparing spatial resolution with producer's and user's accuracies across all classes, along with a linear best-fit line for both sets of points.

Patterns and Spatial Analysis

Subpixel analysis shows substantial variability across superpixels, with pixels classified as unhealthy trees often containing high percentages of herbaceous subpixels within them (Figure 11). There is rarely overclassification based on subpixel percentages, although Sentinel-2 shows overclassification at lower levels of disturbance, the opposite as to what was expected. Additionally, the accuracy differences across scales make comparisons difficult, but there are numerous regions where artificially aggregated unhealthy tree pixels and coarse resolution classifications match (Figure 12). Percentage of unhealthy trees were not consistent with resolution, both when calculated as a percentage of total cover and percentage of forest-classified pixels. Frohn & Hao (2006) have previously evaluated changes in other spatial patterns with

changes in pixel size, such as edge density decreasing as spatial resolution increases. The combination of all unhealthy trees and all mortality agents into one class may result in overlapping of distinct patterns, although disturbances such as drought and insect mortality can co-occur spatially as well (Anderegg et al., 2015).

Classified and quantified patterns are influenced by the life cycle of bark beetles. Once established on one particular tree, the adult insects will release pheromones attracting more beetles to that location, increasing the likelihood of infestation of a neighboring tree, when the beetles will again breed and raise their larvae (Gibson et al., 2009). If attacks are successful, this results in distinct clusters of tree mortality across the forest landscape. For defoliators such as western spruce budworm, adults may lay eggs near where they originally matured, then travel kilometers away from that site (Nealis & Régnière, 2021), depending on conditions. This would also result in patches of mortality surrounded by healthy trees.

Table 5. Summary of the benefits, drawbacks, and management uses of each of the sensors analyzed with regards to tree detection ability and modelling accuracy.

Sensor	Benefit(s)	Drawback(s)	Management Use(s)
MicaSense	<ul style="list-style-type: none"> • Inspect and assess individual tree crowns and damage (diffuse disturbance) • Partial crown disturbance (topkill) • Control over when imagery is collected 	<ul style="list-style-type: none"> • Lower overall accuracy (especially herbaceous at 82%) • Higher within-class variability • Flight mission permission and field accessibility 	<ul style="list-style-type: none"> • Down woody debris detection • Hazard tree management • Detection of diffuse mortality
WorldView-3	<ul style="list-style-type: none"> • Tree crowns match pixel size, able to detect diffuse tree mortality • Covers larger area than UAV acquisition areas 	<ul style="list-style-type: none"> • Tree shadows still impact imagery • Imagery might include cloud cover • Tasking of image acquisition 	<ul style="list-style-type: none"> • Generalized crown-level analysis • Easier separation of classes
Sentinel-2	<ul style="list-style-type: none"> • Generally high accuracy (88% to 100% producer's) • Easy to use across larger, regional scale • Increased sensitivity to detect disturbance 	<ul style="list-style-type: none"> • Difficult to classify without higher resolution data • Loss of fine details • More bands available but have different spatial resolutions 	<ul style="list-style-type: none"> • Observing stand-level events
Landsat 9	<ul style="list-style-type: none"> • Consistently high accuracy (95% to 100% producer's) • Easy to use across larger, regional scale 	<ul style="list-style-type: none"> • Very difficult to classify without higher resolutions • Loss of most details • No diffuse mortality detection 	<ul style="list-style-type: none"> • Severe beetle outbreaks • Whole forest management

Caveats and Improvements

These analyses were designed to act as a case study, showcasing the positives and negatives of different modeling techniques and remote sensors. However, due to this study design, the results shown above are only from one study area, and thus are difficult to extend directly to other forest ecosystems, although it may be possible to gather general trends. The study sites for MicaSense Flights 1 and 2 combined are still very small in area compared to sites covered by foot and especially when compared to an entire satellite image swath. Additionally, disturbances from multiple species of insect, along with other disturbance agents, were not separated in this study, as Stahl et al. (2023) suggests is possible with remote sensing technology. Instead, I grouped all trees affected by any disturbance as unhealthy trees. One factor that impedes the ability to assign disturbance types to disturbance agent is the lack of multitemporal analysis. The patterns of mortality over not just space but also time provides another variable to possibly improve classification and species attribution.

Viewing angles, clouds and shadows, and distortions due to instrument angles all make comparison between scales difficult. Separating trees into red and gray classes may improve classification ability and forest patterns but makes coarser imagery less usable. Coarser resolutions also combine multiple classes together more frequently, which may be partially resolved by using spectral mixing models to capture fraction of green and unhealthy trees within a given pixel (Small, 2004). Corroboration at different scales is also made more difficult by topography in imagery, which may cause significant errors in georeferencing if the portion of the satellite image is sufficiently off-nadir and causes differences in the placement of shadows.

Management Implications

Outbreaks may be better managed by the thinning of forest stands to promote individual growth, particularly for bark beetles such as mountain pine beetle (Fettig et al., 2007). When discussing disturbance and forest management, it is important to consider the aspect of resilience, the ability for an ecosystem to recover and return to pre-disturbance conditions or seral states. There are many different methods of manipulating tree growth to meet management and resilience needs. For instance, creating a mixture of clumps of trees with open areas leads to more susceptibility to insect attacks than other forest management methods, such as basal area and spacing, but then may allow for quicker recovery and growth post-infestation (Churchill et al., 2013). Detecting clusters of already damaged trees will allow for more informed management decisions. Dispersed mortality will likely only be detected at very fine resolutions, while more accurate (in terms of classification) studies can be conducted at whole-forest scales. As a whole, these coarser resolution studies may overestimate abundance of unhealthy trees, while underestimating extents when compared to certain finer resolution severities.

Comparisons and Future Research

In the imagery with finer than 5-m spatial resolution (i.e., UAV imagery as well as WorldView-3), on-screen interpretation can resolve individual trees and thus can better capture dispersed mortality (Figure 8), such as single tree mortality, whereas in coarser resolution we can only capture plot-level (groups of trees) mortality and might overclassify mortality (i.e., when a pixel is not 100% covering affected trees); see Figures 8 and 12. Meddens et al. (2011) suggests that a resolution where a pixel approximately matches the size of a tree crown is beneficial for classification accuracy, and here we see finer resolutions not being correlated with higher overall or specific class accuracy. Future studies focusing on total carbon stocks in forest may find

utility in using drones to complete analyses, as they can detect individual tree patterns and down woody debris that other sensors miss. Using DEMs, either from UAVs or satellites, may assist in classification separation, especially in areas such as this where terrain interference becomes an issue at times. More studies are also needed on methods to improve distinction between trees and herbaceous plants for classification; a fusion of lidar data and multispectral imagery may help here as well. Finally, controlled greenhouse studies on defoliation patterns, spectroscopy, and subsequent detection analysis will not only help field crews recording information, but also GIS analysts working to understand the patterns and processes governing changes in forest health. However, rearing these insects can be difficult, and they may escape these controlled environments or not attack the study trees at all.

CONCLUSION

Research Questions Revisited

(1) What species and size of tree are most affected in the study area, and how well does field data match with UAV data?

Few fully red-attack trees were recorded in study area field plots, but over 10% of trees recorded within plots had some level of topkill. Subalpine fir was noted as having significantly more trees with fewer green needles, but tree health status did not appear to be affected by DBH. While whole tree analysis is possible at both MicaSense and WorldView-3 scales, while sub-crown and debris detection only is feasible with spatial resolutions less than 1 meter (MicaSense-level). Field data does match UAV data in some cases, but overall correlation is weak and sample size is small. More analysis is needed on a wider study area.

(2) Is a parametric or non-parametric model better at classifying satellites for forest health?

A non-parametric model (random forest) consistently outperformed a parametric model (maximum likelihood), even in tests where explanatory variable input was limited in the latter. This may be due to random forest better handling complex variable interactions.

(3) How does spatial resolution affect classification model accuracy?

Overall classification accuracy increased and variability of producer's and user's accuracy across all classes decreased with coarser spatial resolution. This may be due to increase spectral heterogeneity of classes at very fine resolutions.

(4) What spectral bands or indices are most important in classification?

The most important spatial bands or indices were not consistent across different sensors, although the NIR band was in the top five most important variables for the random forest model across all sensors analyzed, and the red band was regularly in the middle of the list of relative variable importance.

(5) Are coarser resolution satellites overestimating or underestimating disturbance, and if so, at what thresholds?

When both WorldView-3 and Sentinel-2 are aggregated to Landsat 9-sized pixels, most unhealthy tree subpixel percentage groups showed underestimation (i.e., lower frequency of unhealthy tree superpixels than expected). Both sensors did not have a sigmoid curve describing the relationship between the quantitative and categorical values of the superpixel to subpixel relationship, and thus thresholds as hypothesized cannot be easily determined. The best estimation of Sentinel-2 imagery compared to finer resolution imagery occurred at 10% to 30% subpixel unhealthy tree occurrence. However, when viewed at a landscape scale, coarser resolution Sentinel-2 predicts a higher percentage of unhealthy trees than finer resolution WorldView-3. This is true for both percentage of unhealthy trees out of all classes and just out of pixels classified as forest. A distribution of subpixel unhealthy tree percentages within superpixels heavily skewed to the right may account for this pattern.

(6) Are landscape metrics consistent across spatial resolutions and scales?

Unhealthy tree patch size, both as percentage of total area and percentage of forest, was not consistent across sensors or selected areas. However, differences in shadow and cloud abundance makes direct comparison difficult.

Main Takeaways

Overall, the type of imagery used must match the natural resource needs and subject of interest. For small stands of trees or individual trees, drone-based or other very high-resolution imagery is feasible and produces reliable and detailed results. Many trees in the study area showed partial damage, dieback, or defoliation on the ground, which was only picked up by the MicaSense data (Figure 8). In other words, individual tree detail was lost when moving from the approximately 0.1-m resolution of a UAV to the approximately 2-meter resolution of some satellites. However, finding individual trees for assessment, hazard level, etc. may not always be wanted or even needed, and thus for more broad scale, stand-level analysis, the very high-resolution satellites may still be helpful. This is especially true for recording topographic changes and or filling in gaps where cloud cover and strong shadows exist. For forest-level analysis, high- or even moderate-resolution satellite imagery may be helpful, although the patterns in these images may be from stands themselves rather than individual trees as spatial resolution decreases. Forest managers should also be aware of the consistent inclusion of other land classes within a coarser-resolution unhealthy tree superpixel. However, depending on the type of mortality agent, such as gap-forming root disease pockets, or the severity of the mortality event, like what would occur with aggregated bark beetle mortality, detection and classification may function well at coarser spatial resolutions. The overall accuracies, as well as most producer's and user's accuracies, were very high for random forest classifications, and this excellent non-parametric model performance should be emphasized for future studies.

REFERENCES

- Acker, S. A., Boetsch, J. R., Fallon, B., & Denn, M. (2023). Stable background tree mortality in mature and old-growth forests in western Washington (NW USA). *Forest Ecology and Management*, 532, 120817. <https://doi.org/10.1016/j.foreco.2023.120817>
- Adams, H. D., Luce, C. H., Breshears, D. D., Allen, C. D., Weiler, M., Hale, V. C., Smith, A. M. S., & Huxman, T. E. (2012). Ecohydrological consequences of drought- and infestation-triggered tree die-off: Insights and hypotheses. *Ecohydrology*, 5(2), 145–159. <https://doi.org/10.1002/eco.233>
- Alfaro, R. I. (1986). Mortality and top-kill in Douglas-fir following defoliation by the western spruce budworm in British Columbia. *Journal of the Entomological Society of British Columbia*, 83, 19–26.
- Allen, C. D., Macalady, A. K., Chenchouni, H., Bachelet, D., McDowell, N., Vennetier, M., Kitzeberger, T., Rigling, A., Breshears, D. D., Hogg, E. H. (Ted), Gonzalez, P., Fensham, R., Zhang, Z., Castro, J., Demidova, N., Lim, J.-H., Allard, G., Running, S. W., Semerci, A., & Cobb, N. (2010). A global overview of drought and heat-induced tree mortality reveals emerging climate change risks for forests. *Forest Ecology and Management*, 259(4), 660–684. <https://doi.org/10.1016/j.foreco.2009.09.001>
- Anderegg, W. R. L., Hicke, J. A., Fisher, R. A., Allen, C. D., Aukema, J., Bentz, B., Hood, S., Lichstein, J. W., Macalady, A. K., McDowell, N., Pan, Y., Raffa, K., Sala, A., Shaw, J. D., Stephenson, N. L., Tague, C., & Zeppel, M. (2015). Tree mortality from drought, insects, and their interactions in a changing climate. *New Phytologist*, 208(3), 674–683. <https://doi.org/10.1111/nph.13477>

- Anderegg, W. R. L., Martinez-Vilalta, J., Cailleret, M., Camarero, J. J., Ewers, B. E., Galbraith, D., Gessler, A., Grote, R., Huang, C., Levick, S. R., Powell, T. L., Rowland, L., Sánchez-Salguero, R., & Trotsiuk, V. (2016). When a Tree Dies in the Forest: Scaling Climate-Driven Tree Mortality to Ecosystem Water and Carbon Fluxes. *Ecosystems*, *19*(6), 1133–1147. <https://doi.org/10.1007/s10021-016-9982-1>
- Baker, W. L. (1994). Restoration of Landscape Structure Altered by Fire Suppression. *Conservation Biology*, *8*(3), 763–769. <https://doi.org/10.1046/j.1523-1739.1994.08030763.x>
- Belgiu, M., & Drăguț, L. (2016). Random forest in remote sensing: A review of applications and future directions. *ISPRS Journal of Photogrammetry and Remote Sensing*, *114*, 24–31. <https://doi.org/10.1016/j.isprsjprs.2016.01.011>
- Bergmüller, K. O., & Vanderwel, M. C. (2022). Predicting Tree Mortality Using Spectral Indices Derived from Multispectral UAV Imagery. *Remote Sensing*, *14*(9), 2195. <https://doi.org/10.3390/rs14092195>
- Breiman, L. (2001). Random Forests. *Machine Learning*, *45*(1), 5–32. <https://doi.org/10.1023/A:1010933404324>
- Breshears, D. D., López-Hoffman, L., & Graumlich, L. J. (2011). When Ecosystem Services Crash: Preparing for Big, Fast, Patchy Climate Change. *AMBIO*, *40*(3), 256–263. <https://doi.org/10.1007/s13280-010-0106-4>
- Bugwood Image Database System*. (2013). <https://images.bugwood.org/>.
- Campbell, M. J., Williams, J. P., & Berryman, E. M. (2023). Using Remote Sensing and Climate Data to Map the Extent and Severity of Balsam Woolly Adelgid Infestation in Northern Utah, USA. *Forests*, *14*(7), 1357. <https://doi.org/10.3390/f14071357>

- Churchill, D. J., Larson, A. J., Dahlgreen, M. C., Franklin, J. F., Hessburg, P. F., & Lutz, J. A. (2013). Restoring forest resilience: From reference spatial patterns to silvicultural prescriptions and monitoring. *Forest Ecology and Management*, 291, 442–457. <https://doi.org/10.1016/j.foreco.2012.11.007>
- Cigan, P. W., Karst, J., Cahill, J. F., Sywenky, A. N., Pec, G. J., & Erbilgin, N. (2015). Influence of bark beetle outbreaks on nutrient cycling in native pine stands in western Canada. *Plant and Soil*, 390(1–2), 29–47. <https://doi.org/10.1007/s11104-014-2378-0>
- Coops, N., Stanford, M., Old, K., Dudzinski, M., Culvenor, D., & Stone, C. (2003). Assessment of Dothistroma Needle Blight of *Pinus radiata* Using Airborne Hyperspectral Imagery. *Phytopathology*®, 93(12), 1524–1532. <https://doi.org/10.1094/PHTO.2003.93.12.1524>
- Curtis, P. G., Slay, C. M., Harris, N. L., Tyukavina, A., & Hansen, M. C. (2018). Classifying drivers of global forest loss. *Science*, 361(6407), 1108–1111. <https://doi.org/10.1126/science.aau3445>
- David M. Smith, Bruce C. Larson, M.J. Kelty, & P. Mark .S. Ashton. (1997). *The practice of silviculture: Applied forest ecology* (9th ed). Wiley.
- De Petris, S., Boccardo, P., & Borgogno-Mondino, E. (2019). Detection and characterization of oil palm plantations through MODIS EVI time series. *International Journal of Remote Sensing*, 40(19), 7297–7311. <https://doi.org/10.1080/01431161.2019.1584689>
- Dello, K. (2017). Prepare for larger, longer wildfires. *Nature*. <https://doi.org/10.1038/nature.2017.22821>
- DeVasto, M. A., Czeck, D. M., & Bhattacharyya, P. (2012). Using image analysis and ArcGIS® to improve automatic grain boundary detection and quantify geological images. *Computers & Geosciences*, 49, 38–45. <https://doi.org/10.1016/j.cageo.2012.06.005>

- Durgun, Y. Ö., Gobin, A., Duveiller, G., & Tychon, B. (2020). A study on trade-offs between spatial resolution and temporal sampling density for wheat yield estimation using both thermal and calendar time. *International Journal of Applied Earth Observation and Geoinformation*, 86, 101988. <https://doi.org/10.1016/j.jag.2019.101988>
- Edburg, S. L., Hicke, J. A., Brooks, P. D., Pendall, E. G., Ewers, B. E., Norton, U., Gochis, D., Gutmann, E. D., & Meddens, A. J. (2012). Cascading impacts of bark beetle-caused tree mortality on coupled biogeophysical and biogeochemical processes. *Frontiers in Ecology and the Environment*, 10(8), 416–424. <https://doi.org/10.1890/110173>
- Esri (2023). [Computer software], *ArcGIS Pro* (2.9.1), <https://www.esri.com/en-us/arcgis/products/arcgis-pro/overview>
- European Space Agency. (2023). *Sentinel-2 S2 Products*. SentiWiki., <https://sentinel.esa.int/web/sentinel/home>
- Evans, J. S., Murphy, M. A., Holden, Z. A., & Cushman, S. A. (2011). Modeling Species Distribution and Change Using Random Forest. In C. A. Drew, Y. F. Wiersma, & F. Huettmann (Eds.), *Predictive Species and Habitat Modeling in Landscape Ecology* (pp. 139–159). Springer New York. https://doi.org/10.1007/978-1-4419-7390-0_8
- Fettig, C. J., Klepzig, K. D., Billings, R. F., Munson, A. S., Nebeker, T. E., Negrón, J. F., & Nowak, J. T. (2007). The effectiveness of vegetation management practices for prevention and control of bark beetle infestations in coniferous forests of the western and southern United States. *Forest Ecology and Management*, 238(1–3), 24–53. <https://doi.org/10.1016/j.foreco.2006.10.011>
- Fox, E. W., Hill, R. A., Leibowitz, S. G., Olsen, A. R., Thornbrugh, D. J., & Weber, M. H. (2017). Assessing the accuracy and stability of variable selection methods for random

- forest modeling in ecology. *Environmental Monitoring and Assessment*, 189(7), 316.
<https://doi.org/10.1007/s10661-017-6025-0>
- Frohn, R. C. (1997). *Remote Sensing for Landscape Ecology: New Metric Indicators for Monitoring, Modeling, and Assessment of Ecosystems* (1st ed.). CRC Press.
<https://doi.org/10.1201/9780203740873>
- Frohn, R., & Hao, Y. (2006). Landscape metric performance in analyzing two decades of deforestation in the Amazon Basin of Rondonia, Brazil. *Remote Sensing of Environment*, 100(2), 237–251. <https://doi.org/10.1016/j.rse.2005.10.026>
- Furniss, R. L., & Carolin, V. M. (1977). *Western Forest Insects* (Miscellaneous Publication No. 1339).
- Gibson, K., Kegley, S. and Bentz, B. (2009). *Mountain pine beetle*. USDA Forest Service, Forest Insect and Disease Leaflet 2.
- Hadney, K. S., & Veblen, T. T. (1992). Stand response to western spruce budworm and Douglas-fir bark beetle outbreaks, Colorado Front Range. *Canadian Journal of Forest Research*, 23.
- Hammond, W. M., Williams, A. P., Abatzoglou, J. T., Adams, H. D., Klein, T., López, R., Sáenz-Romero, C., Hartmann, H., Breshears, D. D., & Allen, C. D. (2022). Global field observations of tree die-off reveal hotter-drought fingerprint for Earth’s forests. *Nature Communications*, 13(1), 1761. <https://doi.org/10.1038/s41467-022-29289-2>
- Hessburg, P. F., Smith, B. G., Salter, R. B., Ottmar, R. D., & Alvarado, E. (2000). Recent changes (1930s–1990s) in spatial patterns of interior northwest forests, USA. *Forest Ecology and Management*, 136(1–3), 53–83. [https://doi.org/10.1016/S0378-1127\(99\)00263-7](https://doi.org/10.1016/S0378-1127(99)00263-7)

- Hicke, J. A., Johnson, M. C., Hayes, J. L., & Preisler, H. K. (2012). Effects of bark beetle-caused tree mortality on wildfire. *Forest Ecology and Management*, 271, 81–90.
- Huang, J., Kautz, M., Trowbridge, A. M., Hammerbacher, A., Raffa, K. F., Adams, H. D., Goodsman, D. W., Xu, C., Meddens, A. J. H., Kandasamy, D., Gershenson, J., Seidl, R., & Hartmann, H. (2020). Tree defence and bark beetles in a drying world: Carbon partitioning, functioning and modelling. *New Phytologist*, 225(1), 26–36.
<https://doi.org/10.1111/nph.16173>
- Immitzer, M., Atzberger, C., & Koukal, T. (2012). Tree Species Classification with Random Forest Using Very High Spatial Resolution 8-Band WorldView-2 Satellite Data. *Remote Sensing*, 4(9), 2661–2693. <https://doi.org/10.3390/rs4092661>
- Jackson, R. D., & Huete, A. R. (1991). Interpreting vegetation indices. *Preventive Veterinary Medicine*, 11(3–4), 185–200. [https://doi.org/10.1016/S0167-5877\(05\)80004-2](https://doi.org/10.1016/S0167-5877(05)80004-2)
- Kiefer, J., & Wolfowitz, J. (1956). Consistency of the Maximum Likelihood Estimator in the Presence of Infinitely Many Incidental Parameters. *The Annals of Mathematical Statistics*, 27(4), 887–906.
- Kurz, W. A., Stinson, G., Rampley, G. J., Dymond, C. C., & Neilson, E. T. (2008). Risk of natural disturbances makes future contribution of Canada’s forests to the global carbon cycle highly uncertain. *Proceedings of the National Academy of Sciences*, 105(5), 1551–1555. <https://doi.org/10.1073/pnas.0708133105>
- Lewis, S. A., Hudak, A. T., Robichaud, P. R., Morgan, P., Satterberg, K. L., Strand, E. K., Smith, A. M. S., Zamudio, J. A., & Lentile, L. B. (2017). Indicators of burn severity at extended temporal scales: A decade of ecosystem response in mixed-conifer forests of

western Montana. *International Journal of Wildland Fire*, 26(9), 755–771.

<https://doi.org/10.1071/WF17019>

Liang, L., Li, X., Huang, Y., Qin, Y., & Huang, H. (2017). Integrating remote sensing, GIS and dynamic models for landscape-level simulation of forest insect disturbance. *Ecological Modelling*, 354, 1–10. <https://doi.org/10.1016/j.ecolmodel.2017.03.007>

Linder, G., Hazelwood, R., Palawski, D., Malloy, J., Dubois, K., Bollman, M., Wilborn, D., Ott, S., Pascoe, G., & Dalsoglio, J. (1994). Ecological assessment for the wetlands at Milltown Reservoir, Missoula, Montana: Characterization of emergent and upland habitats. *Environmental Toxicology and Chemistry*, 13(12), 1957–1970.

<https://doi.org/10.1002/etc.5620131210>

MacLean, D. A. (2016). Impacts of insect outbreaks on tree mortality, productivity, and stand development. *The Canadian Entomologist*, 148(S1), S138–S159.

<https://doi.org/10.4039/tce.2015.24>

Martinuzzi, S., Vierling, L. A., Gould, W. A., Falkowski, M. J., Evans, J. S., Hudak, A. T., & Vierling, K. T. (2009). Mapping snags and understory shrubs for a LiDAR-based assessment of wildlife habitat suitability. *Remote Sensing of Environment*.

MAXAR. (2020). *WorldView-3 Data Sheet*. MAXAR Technologies.

<https://resources.maxar.com/data-sheets/worldview-3>

Maximilian H.K. Hesselbarth, Marco Sciaini, Jakub Nowosad, Sebastian Hanss, Laura J. Graham, Jeffrey Hollister, Kimberly A. With, Florian Privé, Project Nayuki, & Matt Strimas-Mackey. (2023). *Package 'landscapemetrics.'*

- Meddens, A. J. H., Hicke, J. A., & Ferguson, C. A. (2012). Spatiotemporal patterns of observed bark beetle-caused tree mortality in British Columbia and the western United States. *Ecological Applications*, 22(7), 1876–1891. <https://doi.org/10.1890/11-1785.1>
- Meddens, A. J. H., Hicke, J. A., & Vierling, L. A. (2011). Evaluating the potential of multispectral imagery to map multiple stages of tree mortality. *Remote Sensing of Environment*, 115(7), 1632–1642. <https://doi.org/10.1016/j.rse.2011.02.018>
- Meddens, A. J. H., Hicke, J. A., Vierling, L. A., & Hudak, A. T. (2013). Evaluating methods to detect bark beetle-caused tree mortality using single-date and multi-date Landsat imagery. *Remote Sensing of Environment*, 132, 49–58. <https://doi.org/10.1016/j.rse.2013.01.002>
- Meigs, G. W., Kennedy, R. E., & Cohen, W. B. (2011). A Landsat time series approach to characterize bark beetle and defoliator impacts on tree mortality and surface fuels in conifer forests. *Remote Sensing of Environment*, 115(12), 3707–3718. <https://doi.org/10.1016/j.rse.2011.09.009>
- MicaSense, Inc. (2020). *RedEdge-MX Integration Guide*. MicaSense. <https://support.micasense.com/hc/en-us/articles/360011389334-RedEdge-MX-Integration-Guide>
- Mikkelsen, K. M., Bearup, L. A., Maxwell, R. M., Stednick, J. D., McCray, J. E., & Sharp, J. O. (2013). Bark beetle infestation impacts on nutrient cycling, water quality and interdependent hydrological effects. *Biogeochemistry*, 115(1–3), 1–21. <https://doi.org/10.1007/s10533-013-9875-8>
- Nealis, V., & Régnie, J. (2021). *Ecology of outbreak populations of the western spruce budworm*. 12.

- Neigh, C. S. R., Tucker, C. J., Carroll, M. L., Montesano, P. M., Slayback, D. A., Wooten, M. R., Lyapustin, A. I., Shean, D. E., Alexandrov, O., & Macander, M. J. (2019). An API for Spaceborne Sub-Meter Resolution Products for Earth Science. *IGARSS 2019 - 2019 IEEE International Geoscience and Remote Sensing Symposium*, 5397–5400.
<https://doi.org/10.1109/IGARSS.2019.8898358>
- Parker, T. J., Clancy, K. M., & Mathiasen, R. L. (2006). Interactions among fire, insects and pathogens in coniferous forests of the interior western United States and Canada. *Agricultural and Forest Entomology*, 8(3), 167–189. <https://doi.org/10.1111/j.1461-9563.2006.00305.x>
- Pederson, G. T., Graumlich, L. J., Fagre, D. B., Kipfer, T., & Muhlfeld, C. C. (2010). A century of climate and ecosystem change in Western Montana: What do temperature trends portend? *Climatic Change*.
- PRISM 30-Year Normals. (2023). Northwest Alliance for Computational Science and Engineering. <https://prism.oregonstate.edu/normals/>
- R Core Team (2021). R: A language and environment for statistical computing. R Foundation for Statistical Computing, Vienna, Austria. <https://www.R-project.org/>.
- Rhodes, M. W., Bennie, J. J., Spalding, A., French-Constant, R. H., & Maclean, I. M. D. (2022). Recent advances in the remote sensing of insects. *Biological Reviews*, 97(1), 343–360.
<https://doi.org/10.1111/brv.12802>
- Senf, C., Pflugmacher, D., Wulder, M. A., & Hostert, P. (2015). Characterizing spectral–temporal patterns of defoliator and bark beetle disturbances using Landsat time series. *Remote Sensing of Environment*, 170, 166–177. <https://doi.org/10.1016/j.rse.2015.09.019>

- Senf, C., Seidl, R., & Hostert, P. (2017). Remote sensing of forest insect disturbances: Current state and future directions. *International Journal of Applied Earth Observation and Geoinformation*, 60, 49–60. <https://doi.org/10.1016/j.jag.2017.04.004>
- Sisodia, P. S., Tiwari, V., & Kumar, A. (2014). Analysis of Supervised Maximum Likelihood Classification for remote sensing image. *International Conference on Recent Advances and Innovations in Engineering (ICRAIE-2014)*, 1–4. <https://doi.org/10.1109/ICRAIE.2014.6909319>
- Small, C. (2004). The Landsat ETM+ spectral mixing space. *Remote Sensing of Environment*, 93(1–2), 1–17. <https://doi.org/10.1016/j.rse.2004.06.007>
- Stahl, A. T., Andrus, R., Hicke, J. A., Hudak, A. T., Bright, B. C., & Meddens, A. J. H. (2023). Automated attribution of forest disturbance types from remote sensing data: A synthesis. *Remote Sensing of Environment*, 285, 113416. <https://doi.org/10.1016/j.rse.2022.113416>
- Swanson, M. E., Studevant, N. M., Campbell, J. L., & Donato, D. C. (2014). Biological associates of early-seral pre-forest in the Pacific Northwest. *Forest Ecology and Management*, 324, 160–171. <https://doi.org/10.1016/j.foreco.2014.03.046>
- Tilman, D., Reich, P., Phillips, H., Menton, M., Patel, A., Vos, E., Peterson, D., & Knops, J. (2000). Fire Suppression and Ecosystem Carbon Storage. *Ecology*, 81(10), 2680–2685. [https://doi.org/10.1890/0012-9658\(2000\)081\[2680:FSAECS\]2.0.CO;2](https://doi.org/10.1890/0012-9658(2000)081[2680:FSAECS]2.0.CO;2)
- Torres-Sánchez, J., López-Granados, F., & Peña, J. M. (2015). An automatic object-based method for optimal thresholding in UAV images: Application for vegetation detection in herbaceous crops. *Computers and Electronics in Agriculture*, 114, 43–52. <https://doi.org/10.1016/j.compag.2015.03.019>

- Turner, D., Lucieer, A., & Watson, C. (2011). Development of an Unmanned Aerial Vehicle (UAV) for hyper resolution vineyard mapping based on visible, multispectral, and thermal imagery. *Proceedings of 34th International Symposium on Remote Sensing of Environment*, 4.
- United States Geological Survey Landsat Missions. (2023). *Landsat 9*. USGS. <https://www.usgs.gov/landsat-missions/landsat-9>
- U.S. Department of Agriculture. (n.d.-a). *Forest Insect & Disease Leaflets (FIDLs)*. U.S. Forest Service. <https://www.fs.usda.gov/foresthealth/publications/fidls/index.shtml>
- U.S. Department of Agriculture. (n.d.-b). *Mapping & Reporting—Detection Surveys*. U.S. Forest Service. <https://www.fs.usda.gov/foresthealth/applied-sciences/mapping-reporting/detection-surveys.shtml>
- Wang, J., Sammis, T. W., Gutschick, V. P., Gebremichael, M., Dennis, S. O., & Harrison, R. E. (2010). Review of Satellite Remote Sensing Use in Forest Health Studies. *The Open Geography Journal*, 3(1), 28–42. <https://doi.org/10.2174/1874923201003010028>
- Ward, J. S., Anagnostakis, S. L., & Ferrandino, F. J. (1999). *Stand dynamics in Connecticut hardwood forests: The old series plots (1927-1997)* /. Connecticut Agricultural Experiment Station. <https://doi.org/10.5962/bhl.title.51287>
- Windmuller-Campione, M. A., DeRose, J., & Long, J. N. (2021). Landscape-Scale Drivers of Resistance and Resilience to Bark Beetles: A Conceptual Susceptibility Model. *Forests*, 12(6), 798. <https://doi.org/10.3390/f12060798>
- Wulder, M. A., Dymond, C. C., White, J. C., Leckie, D. G., & Carroll, A. L. (2006). Surveying mountain pine beetle damage of forests: A review of remote sensing opportunities. *Forest Ecology and Management*, 221(1–3), 27–41. <https://doi.org/10.1016/j.foreco.2005.09.021>

- Wulder, M. A., White, J. C., Bentz, B., Alvarez, M. F., & Coops, N. C. (2006). Estimating the probability of mountain pine beetle red-attack damage. *Remote Sensing of Environment*, *101*(2), 150–166. <https://doi.org/10.1016/j.rse.2005.12.010>
- Wulder, M. A., White, J. C., Coops, N. C., & Butson, C. R. (2008). Multi-temporal analysis of high spatial resolution imagery for disturbance monitoring. *Remote Sensing of Environment*, *112*(6), 2729–2740. <https://doi.org/10.1016/j.rse.2008.01.010>
- Yi, C., Hendrey, G., Niu, S., McDowell, N., & Allen, C. D. (2022). Tree mortality in a warming world: Causes, patterns, and implications. *Environmental Research Letters*, *17*(3), 030201. <https://doi.org/10.1088/1748-9326/ac507b>
- Zhou, Y., Zhang, R., Wang, S., & Wang, F. (2018). Feature Selection Method Based on High-Resolution Remote Sensing Images and the Effect of Sensitive Features on Classification Accuracy. *Sensors*, *18*(7), 2013. <https://doi.org/10.3390/s18072013>

APPENDIX

APPENDIX

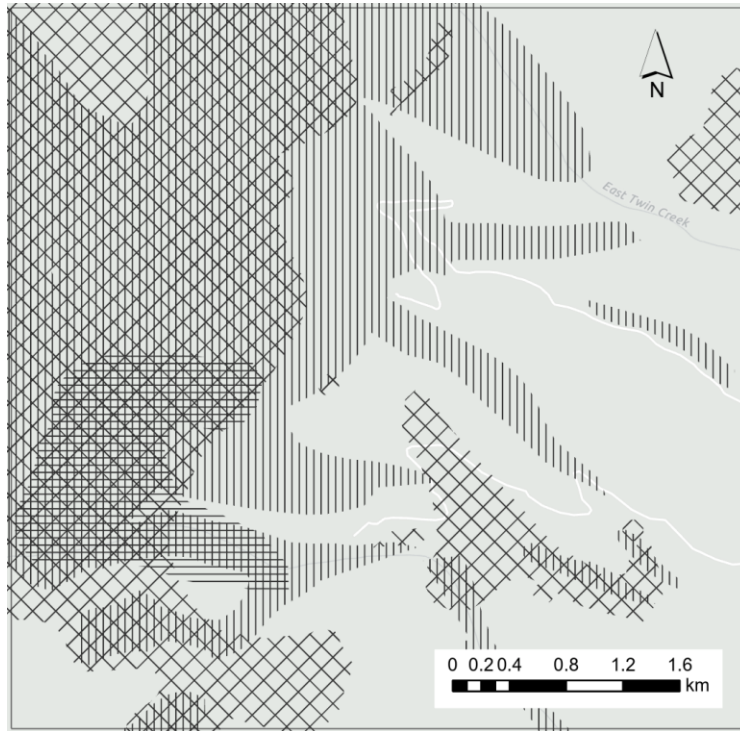


Figure A.1. Study area with IDS polygons from all years shown; horizontal lines are balsam woolly adelgid, vertical lines are western spruce budworm, diagonally cross hatch lines are mountain pine beetle.

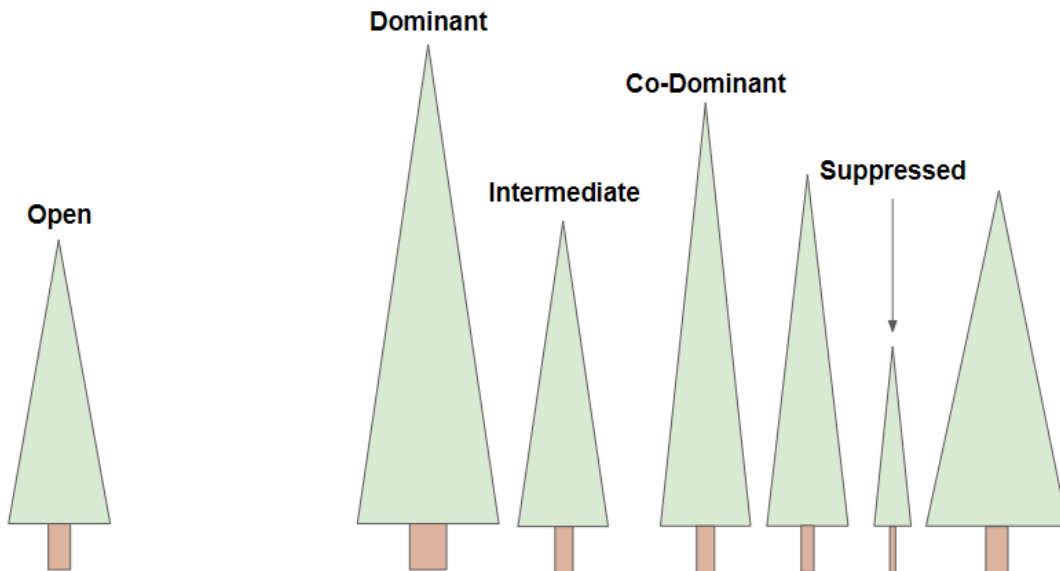


Figure A.2. Diagram of simplified examples for each of the different tree crown class categories used in this study, based on figure by Ward et al., 1999.

After data collection, trees were referenced using a six-digit ID numbering system, with the first two digits assigned to the locality (each site visited is assigned a unique number), the third and fourth digits assigned to the plot number, and the fifth and sixth digits referencing the tree number. For example, tree 01-0307 refers to the seventh tree recorded in plot three from locality number one. Individual trees have 00 as their plot number. The tables below document all relevant data recorded for the trees in the Missoula site. Since all the trees are from the same locality, the first two digits of the tree ID are excluded. See below for abbreviations of variables (left column) and notes (right column), see above chapter for descriptions.

ID: Tree ID	T: Topkill
A: Azimuth (degrees)	I: Minor topkill
D: Distance (m)	B: Broken top
H: Height (m)	M: Moss or lichen on bark
C1: Crown dimension 1 (m)	Q: Sap visible
C2: Crown dimension 2 (m)	G: Stump
CC: Crown class	L: Leaning southeast
S: Status	W: Woodpecker holes
DBH: Diameter at breast height (cm)	B: Webs on trees
HS: Host species	P: Mountain pine beetle damage on fallen tree nearby
G: Percent green	P1: Plot 01-16 moved off of old road
R: Percent red	P2: Plot 01-20 moved off of old road
Y: Percent gray	P3: Plot 01-24 had unhealthy PSME trees nearby
N: Notes	P4: Plot 01-31 moved off road or dried up stream
	P5: Plot 01-37 adjusted away from road
	P6: Plot 01-42 has a PIEN sapling with topkill
	P7: Plot 01-56 in a dead forest with fine branches remaining
	P8: Plot 01-59 is in an area with fire damage, evidence of beetle damage

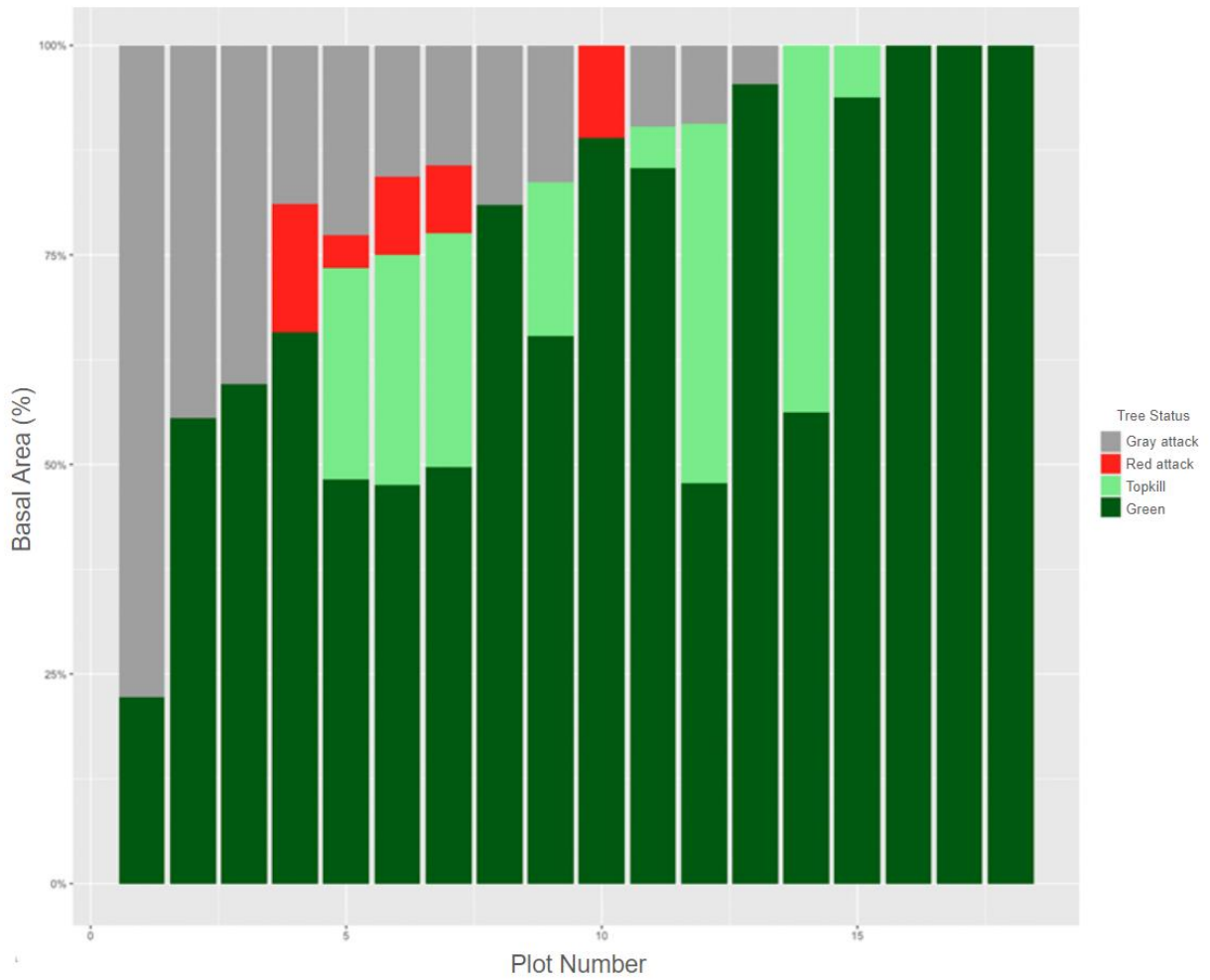


Figure A.3. Proportion of tree basal area with different needle conditions (gray attack, red attack, topkill, or green), sorted by plot.

Table A.1. Individual tree measurements

ID	H	C1	C2	CC	S	DBH	HS	G	R	Y	N
0001	11.8	4.0	4.2	DO	AF	20.4	PICO	80	10	10	
0002	11.3	1.8	1.6	DO	DE	20.3	ABLA	0	0	100	
0003	16.5	3.1	3.7	CO	AF	35.7	ABLA	40	0	60	T,M
0004	13.6	3.7	3.5	DO	AL	26.4	ABLA	90	0	10	M
0005	9.7	2.5	2.3	CO	AF	14.9	ABLA	80	0	20	T
0006	18.2	2.9	3.2	CO	AL	28.3	ABLA	70	0	30	
0007	11.9	5.2	5.3	DO	AL	25.5	PICO	70	0	30	
0008	17.2	5.2	4.6	CO	AL	42.4	PIEN	90	0	10	L
0009	23.1	7.6	7.4	DO	AL	63.7	PSME	90	0	10	L
0010	17.5	3.7	3.7	CO	AF	26.0	ABLA	60	0	40	T
0011	13.2	3.8	3.5	CO	AF	30.4	PSME	70	0	30	
0012	10.2	4.0	3.3	DO	AF	29.1	PSME	70	0	30	T
0013	15.9	6.0	4.9	DO	DE	40.6	PSME	0	0	100	G
0014	12.7	3.8	3.9	DO	DE	29.0	PICO	0	0	100	G
0015	13.2	6.7	5.9	DO	AL	30.3	PICO	90	0	10	
0016	17.8	3.7	3.9	DO	AF	36.1	ABLA	90	0	10	I,Q
0017	7.8	1.5	1.3	CO	AF	13.3	ABLA	0	80	20	T,B,Q
0018	14.5	3.4	4.0	DO	AF	26.3	ABLA	80	0	20	T
0019	12.0	4.3	5.1	CO	AL	19.3	PICO	70	0	30	
0020	14.9	3.2	3.4	CO	AF	25.8	ABLA	0	60	40	Q

Table A.2. Measurements for trees in plots

ID	A	D	CC	S	DBH	HS	G	R	Y	N
1601	18.1	3.2	IN	AF	10.0	ABLA	20	0	80	P1
1602	23.0	3.5	SU	DE	18.3	ABLA	0	0	100	
1603	37.6	5.4	CO	AL	24.0	PSME	80	0	20	
1604	30.9	5.8	SU	DE	10.4	ABLA	0	0	100	
1605	67.5	5.1	IN	DE	15.2	ABLA	0	0	100	
1606	134.8	7.5	DO	AL	42.7	PSME	70	0	30	
1607	160.0	7.0	CO	DE	16.0	ABLA	0	0	100	M
1608	165.3	6.2	IN	DE	13.0	ABLA	0	0	100	M
1609	179.0	6.3	IN	DE	12.3	ABLA	0	0	100	M

1610	186.4	5.8	IN	DE	11.3	ABLA	0	0	100	M
1611	196.3	6.1	IN	AF	13.6	ABLA	30	0	70	
1612	201.3	3.3	CO	AF	25.5	ABLA	50	20	30	T
1613	224.5	7.7	IN	AF	13.5	ABLA	60	0	40	T
1614	228.4	7.7	IN	AF	10.9	ABLA	50	0	50	T
1615	244.4	6.3	CO	AF	16.5	ABLA	40	0	60	T
1616	323.7	7.8	CO	AF	17.6	ABLA	60	0	40	T
1617	357.9	7.6	SU	AF	11.9	ABLA	50	0	50	
1618	4.6	7.8	CO	DE	15.3	ABLA	0	30	70	
1619	1.7	6.8	IN	AL	10.0	PICO	80	0	20	
1901	17.2	7.5	IN	AL	12.8	PSME	90	0	10	
1902	33.3	7.0	SU	AL	11.7	PSME	70	0	30	
1903	42.1	5.5	CO	AL	14.7	PSME	80	0	20	
1904	51.4	6.0	SU	AL	12.2	PSME	60	0	40	
1905	54.4	6.5	CO	AL	15.6	PSME	70	0	30	
1906	98.7	3.0	CO	AL	18.2	PICO	90	0	10	
1907	252.3	5.5	CO	AL	30.4	PICO	70	0	30	
1908	290.7	7.3	CO	AF	29.3	PICO	60	10	30	
1909	349.6	2.8	DO	AF	32.5	PSME	50	0	50	
1910	357.7	6.5	CO	AL	18.5	PICO	70	0	30	
2001	274.1	5.7	IN	DE	19.8	ABLA	0	0	100	P2
2002	202.9	5.6	CO	AL	16.7	PICO	90	0	10	
2003	145.3	6.1	CO	AL	14.5	PICO	100	0	0	
2401	83.4	7.5	CO	AL	42.7	PSME	70	0	30	P3
2402	132.1	0.6	UK	DE	22.9	UK	0	0	100	M
2403	159.5	2.2	IN	AL	15.6	PSME	100	0	0	
2404	264.5	3.9	CO	AL	13.0	PSME	100	0	0	
2501	330.5	5.0	CO	AF	21.2	PIEN	60	0	40	T
2502	330.5	7.3	CO	AF	12.8	ABLA	80	0	20	
2503	353.1	4.8	UK	DE	41.1	ABLA	0	0	100	M
2504	23.2	7.4	CO	AF	35.0	ABLA	30	0	70	T
2505	33.5	4.7	SU	AF	15.2	ABLA	60	0	40	T
2506	49.0	5.0	CO	AF	15.9	ABLA	60	0	40	
2507	56.0	6.3	IN	AL	19.0	PSME	70	0	30	
2508	92.7	3.6	DO	AL	53.0	PIEN	90	0	10	
2509	112.5	6.3	IN	AL	29.3	PSME	60	0	40	
2510	139.3	5.2	CO	AL	32.4	PIEN	60	0	40	
2511	136.3	1.6	CO	AL	35.5	PIEN	80	0	20	

2601	48.5	2.5	CO	AL	10.4	PICO	70	0	30	
2602	67.1	2.4	CO	AL	10.7	PICO	80	0	20	
2603	77.0	4.0	CO	AL	11.0	PICO	70	0	30	
2604	47.7	6.0	CO	AL	12.9	PICO	95	5	0	
2605	74.3	4.6	CO	AL	10.2	PICO	80	0	20	
2606	81.7	5.7	DO	AL	17.7	PICO	90	0	10	
2607	101.0	2.7	DO	AL	12.5	PICO	80	5	15	
2608	112.5	2.3	CO	AL	12.5	PIPO	100	0	0	
2609	152.3	3.5	CO	AL	10.7	PICO	90	0	10	
2610	255.2	3.3	IN	AL	10.9	PICO	90	0	10	
3001	53.5	6.3	CO	AF	20.9	PICO	70	0	30	
3002	73.9	6.5	CO	AF	20.7	PICO	80	0	20	
3003	79.9	7.5	CO	AF	23.9	PICO	60	0	40	
3004	101.4	7.2	CO	AF	22.7	PICO	60	0	40	
3005	218.2	3.9	SU	AL	10.8	PSME	90	0	10	
3006	222.8	3.3	DO	AL	26.1	PSME	90	0	10	
3007	241.4	3.7	IN	AL	16.0	PSME	80	0	20	
3008	280.5	3.3	CO	AL	19.7	PSME	90	0	10	
3101	79.2	7.7	CO	AL	14.9	PICO	90	0	10	P4
3102	89.3	6.5	SU	DE	11.3	PICO	0	0	100	
3103	91.1	5.4	CO	AL	18.8	PICO	80	0	20	
3104	107.5	3.7	CO	AL	13.5	PICO	90	0	10	
3105	110.0	5.1	IN	AL	10.8	PICO	90	0	10	
3106	142.6	6.7	IN	AL	18.1	PICO	70	0	30	
3107	139.5	7.8	DO	AL	25.7	PICO	80	5	15	
3108	145.1	7.8	SU	AL	14.5	PIPO	70	0	30	
3109	161.0	6.7	CO	AF	21.0	PICO	60	0	40	
3110	174.6	5.8	SU	AL	16.9	PSME	90	0	10	
3111	180.7	4.8	CO	AL	17.8	PICO	80	0	20	
3112	195.0	4.2	CO	AL	17.2	PICO	70	0	30	
3113	202.2	6.5	IN	AL	18.3	PSME	70	0	30	W
3114	195.4	7.0	SU	DE	12.7	PICO	0	0	100	G
3115	189.6	7.5	CO	AF	25.2	PICO	60	0	40	
3116	177.5	7.2	IN	AL	17.9	PICO	80	0	20	
3117	173.7	7.5	DO	AL	24.6	PICO	70	10	20	
3118	233.3	7.3	IN	AL	10.2	LAOC	90	0	10	
3119	280.6	4.4	CO	AL	12.0	LAOC	80	0	20	
3120	253.9	4.9	CO	AL	10.5	PICO	90	0	10	

3121	246.5	0.6	DO	AL	17.2	PICO	100	0	0	
3301	272.5	4.3	DO	AL	19.8	PICO	90	0	10	
3302	292.4	4.0	CO	AL	18.1	PICO	80	0	20	
3303	317.9	1.7	IN	AF	13.2	ABLA	10	20	70	
3304	324.0	7.0	CO	AF	20.3	ABLA	10	0	90	
3305	345.1	5.4	IN	AF	16.3	ABLA	60	0	40	
3306	348.6	7.1	DO	AF	16.5	ABLA	60	5	35	
3307	355.2	7.5	IN	AF	11.2	ABLA	60	0	40	
3308	9.1	4.5	CO	AL	12.1	PICO	90	0	10	
3309	3.5	2.6	CO	AL	16.1	PICO	90	5	5	
3310	59.6	5.7	CO	AL	20.8	PICO	90	0	10	
3311	57.4	7.2	CO	AL	23.8	PICO	80	0	20	
3312	119.2	6.1	CO	AL	30.5	PICO	80	0	20	
3313	144.5	5.5	DO	DE	27.8	ABLA	0	70	30	
3314	139.4	7.2	IN	AF	15.3	ABLA	60	0	40	
3315	153.9	7.9	SU	AF	11.4	ABLA	50	0	50	
3316	177.8	6.3	CO	AF	23.3	ABLA	70	0	30	
3317	175.7	3.8	IN	AL	12.4	ABLA	80	0	20	
3318	193.9	7.3	SU	AF	11.7	ABLA	10	0	90	
3319	205.8	7.4	CO	AF	19.0	ABLA	60	0	40	
3320	220.3	7.0	CO	AF	15.6	ABLA	40	0	60	
3321	223.9	7.3	SU	AF	10.4	UK	60	0	40	
3701	31.3	2.5	CO	AF	13.1	PSME	50	0	50	P5
3702	47.1	4.7	CO	AL	11.5	ABLA	80	0	20	
3703	37.9	5.5	SU	AL	11.6	PIEN	70	0	30	
3704	41.3	5.8	DO	AF	16.5	PIEN	80	0	20	T
3705	45.1	5.9	SU	AL	11.9	PIEN	80	0	20	
3706	53.8	6.3	IN	AL	11.9	PIEN	70	0	30	
3707	50.2	7.2	CO	AF	14.6	PIEN	60	0	40	T
3708	58.1	5.8	CO	AF	15.3	ABLA	70	0	30	T
3709	95.1	4.7	CO	AL	14.9	LAOC	70	0	30	
3710	112.2	6.0	DO	AL	14.9	LAOC	80	0	20	
3711	124.2	7.2	IN	AL	14.0	ABLA	80	0	20	
3712	124.8	4.4	CO	AL	11.0	LAOC	60	0	40	
3713	140.9	4.6	CO	AL	11.3	PSME	70	0	30	F
3714	206.9	5.0	CO	AL	12.5	ABLA	70	0	30	
3715	224.3	7.0	CO	AL	12.9	PSME	80	0	20	F
3716	240.2	5.4	CO	AL	10.0	LAOC	80	0	20	

3717	279.0	7.0	CO	AL	15.8	ABLA	70	20	10	
3718	289.4	7.4	SU	AF	13.0	ABLA	30	40	30	T
3719	278.3	2.7	SU	AF	10.0	PSME	80	0	20	T,F
3720	304.5	2.0	DO	AF	24.8	ABLA	70	0	30	T
3721	294.3	1.5	CO	AL	12.8	PIEN	80	0	20	
4201	12.1	6.4	CO	AL	21.5	PICO	90	0	10	P6
4202	16.0	7.8	CO	AL	23.9	PICO	80	0	20	
4203	17.8	7.4	CO	AL	21.2	PICO	90	0	10	
4204	90.2	7.9	CO	DE	10.4	ABLA	0	0	100	
4205	107.9	7.5	DO	AF	12.8	ABLA	70	0	30	T
4206	122.0	2.8	IN	DE	12.8	ABLA	0	0	100	
4207	147.9	6.3	CO	AL	20.4	PICO	80	0	20	
4208	152.0	7.0	SU	AF	10.3	PSME	80	0	20	I
4209	142.4	2.6	CO	AL	17.8	PICO	70	0	30	
4210	193.6	1.8	CO	AL	13.3	PICO	80	0	20	
4211	190.8	3.5	SU	AF	10.2	PICO	70	5	25	
4212	200.7	3.7	DO	AL	26.7	PICO	70	0	30	
4213	207.6	1.9	IN	AL	13.8	PICO	60	0	40	
4214	219.6	3.5	CO	AL	13.5	PICO	80	0	20	
4215	247.1	1.9	CO	AL	15.3	PICO	70	0	30	
4216	238.3	3.7	IN	AL	11.0	PICO	70	0	30	
4217	258.7	3.5	IN	AL	17.4	PICO	70	0	30	
4218	253.3	6.1	CO	DE	16.2	ABLA	0	0	100	
4219	285.7	3.9	DO	AL	21.4	PICO	80	0	20	
5301	11.6	7.0	IN	AF	10.2	ABLA	50	0	50	T
5302	91.1	3.3	CO	AL	10.9	ABLA	80	0	20	
5303	94.7	7.4	IN	AF	16.8	ABLA	60	0	40	T
5304	104.4	5.9	CO	AL	15.6	PICO	90	0	10	
5305	126.4	6.9	SU	AL	11.2	PICO	80	0	20	
5306	123.0	7.8	IN	AL	11.8	PICO	90	0	10	
5307	133.7	7.8	IN	AF	16.2	ABLA	70	0	30	T
5308	167.5	6.6	IN	AL	12.0	PICO	80	0	20	
5309	157.1	3.3	DO	AF	17.5	ABLA	75	0	25	T,M
5310	224.3	4.1	SU	AL	17.2	PICO	90	0	10	
5311	253.3	2.6	CO	DE	14.5	ABLA	0	0	100	
5401	16.9	5.8	CO	AL	10.4	PICO	80	0	20	
5402	34.7	4.5	DO	DE	25.9	PICO	0	0	100	
5403	26.8	7.4	IN	AL	11.6	PICO	90	0	10	

5404	60.9	4.1	CO	AL	12.9	PICO	70	0	30	
5405	75.1	7.4	CO	AL	12.7	PICO	80	0	20	
5406	93.7	4.4	SU	AF	14.4	PICO	40	0	60	Q
5407	94.6	5.3	CO	AF	14.1	PICO	60	0	40	Q
5408	101.7	5.5	SU	AL	11.7	PICO	70	0	30	
5409	120.6	4.4	CO	AL	12.3	PICO	80	0	20	
5410	129.8	7.3	IN	AL	14.2	PICO	70	0	30	
5411	175.9	4.4	CO	AL	15.0	PICO	80	0	20	
5412	177.1	7.6	IN	DE	19.7	PSME	0	0	100	G
5413	263.0	5.3	DO	AL	19.0	PICO	80	0	20	P
5414	289.4	6.0	SU	DE	29.3	ABLA	0	40	60	
5415	302.1	6.2	CO	AF	15.2	PICO	60	10	30	
5416	317.6	6.3	CO	AF	12.6	PICO	50	0	50	
5417	322.1	6.2	CO	AL	10.2	PICO	70	0	30	
5418	312.4	5.2	SU	AF	10.8	PICO	70	0	30	
5419	312.4	5.1	CO	AL	15.0	PICO	70	0	30	
5420	310.8	4.9	SU	AL	11.2	PICO	70	0	30	
5421	322.1	3.0	CO	AL	17.1	PICO	80	0	20	
5422	328.1	5.5	CO	AL	14.3	PICO	80	5	15	
5423	339.7	5.6	IN	AL	13.3	PICO	90	0	10	
5501	12.1	3.4	SU	AL	11.7	PSME	70	0	30	
5502	25.1	3.3	CO	DE	15.7	ABLA	0	40	60	
5503	26.2	6.0	CO	AF	16.6	ABLA	20	30	50	
5504	33.9	7.4	IN	DE	11.1	ABLA	0	30	70	
5505	48.7	4.7	DO	AL	24.1	PICO	70	0	30	
5506	92.8	2.3	CO	DE	19.5	ABLA	0	10	90	
5507	95.7	3.2	CO	AL	18.8	PICO	80	0	20	
5508	126.5	6.6	IN	AF	18.0	ABLA	60	0	40	T
5509	136.0	7.0	SU	AF	15.6	ABLA	30	0	70	
5510	156.8	2.7	SU	DE	12.4	PSME	0	0	100	
5511	180.9	2.6	DO	AL	21.0	PICO	80	0	20	
5512	163.3	4.3	CO	DE	22.5	PSME	0	0	100	
5513	321.1	3.4	IN	AL	10.2	PSME	70	0	30	
5514	321.9	7.1	IN	AL	12.3	PSME	70	0	30	
5515	338.6	7.8	DO	AF	31.0	ABLA	40	10	50	T
5601	330.0	4.6	UK	DE	35.1	PSME	0	0	100	M,P7
5602	19.4	5.4	CO	DE	19.7	ABLA	0	0	100	
5603	18.1	2.2	SU	DE	12.9	ABLA	0	0	100	L

5604	39.5	5.4	DO	DE	33.7	ABLA	0	0	100	
5605	48.6	3.9	CO	AF	28.2	PIEN	80	5	15	
5606	101.8	5.6	IN	DE	12.4	ABLA	0	0	100	G
5607	168.5	2.0	CO	DE	11.3	ABLA	0	0	100	
5608	192.9	2.4	IN	DE	10.3	ABLA	0	0	100	
5609	165.7	5.0	IN	DE	14.8	ABLA	0	0	100	
5610	236.4	3.0	IN	DE	10.0	ABLA	0	0	100	
5611	270.9	4.3	DO	AF	16.7	ABLA	40	0	60	
5612	287.0	8.0	CO	DE	11.4	ABLA	0	0	100	
5701	340.0	4.9	IN	AL	12.2	ABLA	70	0	30	
5702	349.8	3.9	IN	AF	12.2	ABLA	30	0	70	
5703	14.3	2.8	CO	AF	13.4	ABLA	50	10	40	
5704	14.0	4.5	CO	AF	17.5	ABLA	0	10	90	
5705	16.0	5.1	CO	DE	20.8	ABLA	0	0	100	
5706	5.3	6.5	UK	DE	20.8	ABLA	0	0	100	G
5707	8.9	7.8	CO	DE	17.9	ABLA	0	20	80	
5708	50.0	5.6	CO	AL	19.2	ABLA	70	5	25	
5709	48.1	7.2	CO	AF	28.0	ABLA	70	0	30	
5710	56.0	7.5	DO	AF	34.2	ABLA	80	0	20	
5711	61.5	7.8	SU	AF	17.3	ABLA	40	0	60	
5712	74.6	5.7	CO	AF	23.2	ABLA	60	0	40	T
5713	87.4	7.7	IN	DE	17.5	ABLA	0	0	100	G
5714	91.8	7.4	SU	AF	10.6	ABLA	30	0	70	
5715	90.7	2.1	SU	AF	12.6	ABLA	60	0	40	T
5716	45.4	1.2	CO	AL	21.1	ABLA	80	0	20	
5717	113.4	1.8	DO	AF	17.1	PICO	50	0	50	
5718	116.7	6.0	UK	DE	12.6	ABLA	0	0	100	M
5719	123.9	6.2	CO	AF	26.9	PSME	0	30	70	
5720	126.0	6.4	SU	AF	15.1	ABLA	60	0	40	T
5721	128.8	5.0	IN	DE	15.7	ABLA	0	0	100	M
5722	201.4	3.6	DO	AF	32.8	PIEN	80	0	20	
5723	216.1	4.0	SU	AF	17.8	ABLA	70	0	30	T
5724	231.5	0.7	SU	DE	13.8	ABLA	0	0	100	
5725	247.1	1.7	IN	AL	17.8	PIEN	70	0	30	
5726	239.4	6.3	DO	AF	32.3	ABLA	60	0	40	T
5727	289.3	0.5	DO	AF	28.4	ABLA	80	0	20	T
5801	241.2	0.4	CO	AL	16.7	PIPO	60	0	40	
5802	240.4	5.5	DO	AL	23.6	PSME	90	0	10	

5803	281.4	4.0	IN	AF	11.3	PIPO	10	0	90	
5804	307.4	2.6	IN	AL	13.6	PIPO	60	5	35	
5805	318.8	3.0	CO	AL	10.0	LAOC	70	0	30	
5806	324.6	37.7	IN	AL	10.2	LAOC	80	0	20	
5807	330.6	8.0	CO	AL	12.7	LAOC	70	0	30	
5808	335.1	7.9	CO	AL	14.9	PICO	80	0	20	
5809	19.9	7.6	CO	AF	14.9	PSME	80	0	20	T
5810	40.1	5.0	DO	AL	10.7	LAOC	70	0	30	
5811	78.3	6.5	SU	AL	11.7	PSME	80	0	20	
5812	81.7	7.5	DO	AL	21.5	PICO	90	0	10	
5813	103.5	2.1	CO	AL	17.4	PSME	80	0	20	
5814	153.0	6.0	IN	AF	12.9	PIPO	60	5	35	B
5815	153.8	6.4	CO	AL	14.3	PSME	80	0	20	
5816	149.4	7.4	IN	AL	10.0	PIPO	70	0	30	
5817	166.3	6.6	IN	AL	10.7	PSME	90	0	10	
5901	297.4	0.1	IN	DE	18.2	PICO	0	0	100	P8
5902	335.4	1.1	CO	AL	21.0	PICO	UK	UK	UK	
5903	111.8	0.2	CO	DE	25.5	PICO	0	0	100	
5904	85.2	1.8	DO	AF	23.3	PICO	80	0	20	Q
5905	93.4	2.0	SU	AL	10.3	PICO	85	5	10	
5906	116.2	6.9	CO	DE	25.1	PICO	0	0	100	
5907	127.4	6.1	SU	AF	10.2	PSME	70	10	20	
5908	138.0	6.2	CO	AF	18.1	PICO	50	0	50	
5909	154.7	6.8	SU	AF	10.8	PICO	30	0	70	
5910	160.3	6.1	IN	DE	21.1	PICO	0	0	100	
5911	157.9	4.2	CO	DE	21.7	PICO	0	0	100	
5912	170.3	4.7	IN	DE	12.5	PICO	0	0	100	
5913	182.1	4.6	SU	DE	11.0	PICO	0	0	100	
5914	187.3	4.7	IN	DE	14.5	PICO	0	0	100	
5915	187.4	5.7	CO	AL	16.6	PICO	70	0	30	
5916	192.3	5.9	SU	DE	14.0	PICO	0	0	100	
5917	211.5	6.2	CO	DE	18.8	PICO	0	0	100	
5918	211.9	6.8	SU	AF	12.7	PICO	60	0	40	
5919	338.6	7.6	DO	AF	25.7	PICO	60	0	40	
5920	330.0	6.8	SU	AF	11.0	PICO	20	0	80	
5921	330.0	6.5	CO	AF	24.3	PICO	60	0	40	
5922	305.2	7.5	CO	AL	29.0	PICO	80	0	20	
5923	225.8	5.9	IN	AL	24.4	PICO	70	0	30	

5924	36.7	3.1	CO	AL	19.1	LAOC	100	0	0	
------	------	-----	----	----	------	------	-----	---	---	--

Table A.3. Confusion matrix for evaluation data, based on a random forest classification model of MicaSense Flight 1 imagery.

Predicted Class	Actual Class						User's Accuracy
	Green Trees	Unhealthy Trees	Bare Ground	Herbaceous	Shadow	Total	
Green Trees	32	0	0	15	0	47	0.681
Unhealthy Trees	0	34	1	0	0	35	0.971
Bare Ground	0	6	38	0	0	44	0.864
Herbaceous	7	0	1	25	0	33	0.758
Shadow	1	0	0	0	40	41	0.976
Total	40	40	40	40	40	200	0
Producer's Accuracy	0.8	0.85	0.95	0.625	1	0	0.845

Table A.4. Confusion matrix for evaluation data, based on a random forest classification model of MicaSense Flight 2 imagery.

Predicted Class	Actual Class						User's Accuracy
	Green Trees	Unhealthy Trees	Bare Ground	Herbaceous	Shadow	Total	
Green Trees	28	0	0	12	0	40	0.700
Unhealthy Trees	0	36	6	0	1	43	0.837
Bare Ground	0	3	34	0	0	37	0.919
Herbaceous	11	0	0	27	1	39	0.692
Shadow	1	1	0	1	38	41	0.927
Total	40	40	40	40	40	200	0
Producer's Accuracy	0.7	0.9	0.85	0.675	0.95	0	0.815

Table A.5. Confusion matrix for evaluation data, based on a random forest classification model of WorldView-3 imagery.

Predicted Class	Actual Class						User's Accuracy
	Green Trees	Unhealthy Trees	Bare Ground	Herbaceous	Shadow	Total	
Green Trees	34	1	0	1	1	37	0.919
Unhealthy Trees	2	38	1	0	0	41	0.927
Bare Ground	0	0	39	0	0	39	1
Herbaceous	4	0	0	39	0	43	0.907
Shadow	0	1	0	0	39	40	0.975
Total	40	40	40	40	40	200	0
Producer's Accuracy	0.85	0.95	0.975	0.975	0.975	0	0.945

Table A.6. Confusion matrix for evaluation data, based on a random forest classification model of Sentinel-2 imagery.

Predicted Class	Actual Class						User's Accuracy
	Green Trees	Unhealthy Trees	Bare Ground	Herbaceous	Shadow	Total	
Green Trees	37	0	0	0	0	37	1
Unhealthy Trees	1	40	2	0	2	45	0.889
Bare Ground	0	0	35	1	0	36	0.972
Herbaceous	2	0	3	39	0	44	0.886
Shadow	0	0	0	0	38	38	1
Total	40	40	40	40	40	200	0
Producer's Accuracy	0.925	1	0.875	0.975	0.95	0	0.945

Table A.7. Confusion matrix for evaluation data, based on a random forest classification model of Landsat 9 imagery.

Predicted Class	Actual Class						User's Accuracy
	Green Trees	Unhealthy Trees	Bare Ground	Herbaceous	Shadow	Total	
Green Trees	39	0	1	0	0	40	0.975
Unhealthy Trees	0	39	0	0	1	40	0.975
Bare Ground	0	0	38	0	0	38	1.000
Herbaceous	1	0	1	40	0	42	0.952
Shadow	0	1	0	0	39	40	0.975
Total	40	40	40	40	40	200	0
Producer's Accuracy	0.975	0.975	0.95	1	0.975	0	0.975